European Commission

Research Programme of the Research Fund for Coal and Steel

ANGELHY

Innovative solutions for design and strengthening of telecommunications and transmission lattice towers using large angles from high strength steel and hybrid techniques of angles with FRP strips

WORK PACKAGE 2 – DELIVERABLE 2.4

Proposal for design rules for hybrid angle members

Coordinator:

National Technical University of Athens - NTUA, Greece

Beneficiaries:

ArcelorMittal Belval & Differdange SA - AMBD, Luxembourg

Universite de Liege - ULG, Belgium

COSMOTE Kinites Tilepikoinonies AE - COSMOTE, Greece

Centre Technique Industriel de la Construction Metallique - CTICM, France

SIKA France SAS - SIKA, France

Grant Agreement Number: 753993

AUTHORS:

SIKA France SAS
84 rue Edouard Vaillant, 93350 Le Bourget, France
Authors: Yvon Giquel, Sébastien Reygner

NATIONAL TECHNICAL UNIVERSITY OF ATHENS
Institute of Steel Structures
15780 Athens, Greece
Authors: Ioannis Vayas, Konstantinos Vlachakis, Angeliki Gerontati, Evdoxia Karaferi

TABLE OF CONTENTS

1 Introduction 3
2 Cross section properties of hybrid angle profiles 4
2.1 Notation for the steel angle sections 4
2.2 Mechanical properties of a hybrid section composed of a steel angle profile + external FRPs – principal axes 5
2.2.1 Geometrical properties of FRP plates 5
2.2.2 Material properties of FRP plates 5
2.2.3 Cross-section area 5
2.2.4 Position of centroid: 5
2.2.5 Second moment of area, weak axis 6
2.2.6 Second moment of area, strong axis 6
2.2.7 Elastic moment, weak axis 6
2.2.8 Elastic moment, strong axis 6
2.2.9 Limit elastic - plastic moment, weak axis 7
2.2.10 Limit elastic - plastic moment, strong axis 9
2.3 Properties of the hybrid section composed of angle section steel + external and internal FRPs – principal axes 9
2.4 Properties of the hybrid section composed of angle section steel + external FRPs – geometric axes 10
2.4.1 Cross-section area 10
2.4.2 Position of centroid: 10
2.4.3 Second moment of area, ... 11
2.4.4 Elastic moment, tip in tension, leg in compression 11
2.4.5 Elastic moment, leg in tension 11
2.4.6 Elastic-plastic moment, leg in compression 12
2.4.7 Elastic-plastic moment, leg in tension 13
3 Safety factors 15
3.1 General 15
3.2 Partial factors 15
3.3 Conversion factor 16
4 Cross-section design 18
4.1 Cross-section classification 18
4.2 Design resistance to axial force 18
4.2.1 Compression 18
4.2.2 Tension 18
4.3 Design resistance to strong axis bending 18
4.4 Design resistance to weak axis bending 18
4.5 Design resistance to combined effects 18
5 Member design 20
5.1 Compression 20

5.2 Strong axis bending 20
5.3 Weak axis bending 21
5.4 Combined effects – Compression and bending 21
6 Experimental validation 22
6.1 Cross section properties 22
6.1.1 Second moment of area, moment capacity 22
6.1.2 Position of the centroid 27
6.2 Design interaction formulae 31
7 Numerical validation 34
7.1 Modelling with beam elements 34
7.1.1 Bending tests 35
7.1.2 Compression tests 38
7.2 Modelling with FEM using volume elements 42
8 Conclusions 49
References 50
List of Figures 51
List of Tables 54

1 Introduction

Hybrid angle members considered here are composed of equal leg steel angles, strengthened with two FRP plates attached to the exterior side of the legs or with four FRP plates attached to the exterior and interior side of the legs. The width and length of the FRP plates shall be no larger than the corresponding width/length of the angle legs. This report presents the mechanical properties of the hybrid sections and presents design rules to combined forces and moments. The rules are applicable to the hybrid sections studied during the current research project, i.e. rolled angle sections strengthened externally or externally and internally by FRP plates.

2 Cross section properties of hybrid angle profiles

2.1 Notation for the steel angle sections

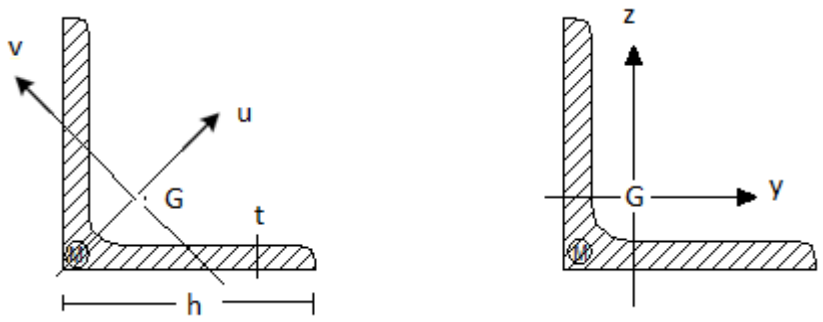

Figure 2.1: Notation, principal and geometric axes for equal angle section

Material properties, steel Figure 2.1

Modulus of elasticity E_s

Limit stress of steel f_s

Yield strength f_y

Ultimate strength f_u

Cross-section properties

Cross-section area A_s

Position of centroid u_{Gs}

Second moments of area $I_{u,s}$ $I_{vs,}$

Plastic section moduli $W_{u,pl,s}$ $W_{v,pl,s}$

Elastic section moduli $W_{u,el,s}$ $W_{v,el,s}$

Plastic moments: $M_{pl,s} = W_{pl,s} \cdot f_y$

Elastic moments: $M_{el,s} = W_{el,s} \cdot f_y$

Warping constant: I_{ws}

Torsion constant: I_{ts}

Polar radius of gyration: $i_{ps} = \sqrt{\frac{I_u + I_v}{A}}$

2.2 Mechanical properties of a hybrid section composed of a steel angle profile + external FRPs – principal axes

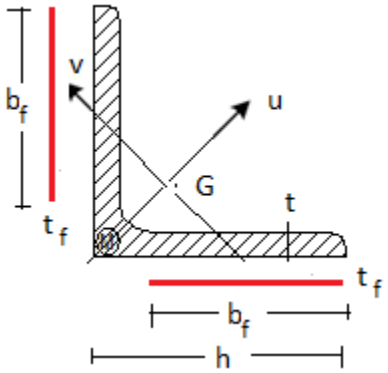

Figure 2.2: Notation and principal axes for hybrid section

2.2.1 Geometrical properties of FRP plates

Width of plate b_f

Thickness of plate t_f

2.2.2 Material properties of FRP plates

Modulus of elasticity E_f

Nominal tensile strength $f_{f,nom}$

Limit strength $f_f = k \cdot f_{f,nom}$

k reduction factor for strength

Modular ratio between steel and FRP material: $n = \frac{E_s}{E_f}$ (2.1)

2.2.3 Cross-section area

Cross-section area of FRP: $A_f = 2 \cdot b_f \cdot t_f$ (2.2)

Cross-section area of equivalent section: $A_i = A_s + A_f/n$ (2.3)

2.2.4 Position of centroid:

FRP section: $u_{Gf} = \left(h - b_f/2\right)/\sqrt{2}$ (2.4)

Equivalent section: $u_{Gi} = \frac{A_s \cdot u_{Gs} + A_f/n \cdot u_{Gf}}{A_i}$ (2.5)

2.2.5 Second moment of area, weak axis

$$I_{vi} = I_{vs} + A_s.(u_{Gi} - u_{Gs})^2 + A_f/n \cdot \left(u_{Gi} - u_{Gf}\right)^2 \quad (2.6)$$

Remark: The FRP plates are considered to contribute only with the Steiner part.

2.2.6 Second moment of area, strong axis

$$I_{ui} = I_{us} + \frac{h^3-(h-b)^3}{3 \cdot n} \cdot t \quad (2.7)$$

Remark: The FRP plates are considered to contribute only with the Steiner part.

2.2.7 Elastic moment, weak axis

The elastic moment is determined from the condition that either steel reaches its yield strength or the FRP plates the correspondent strength.

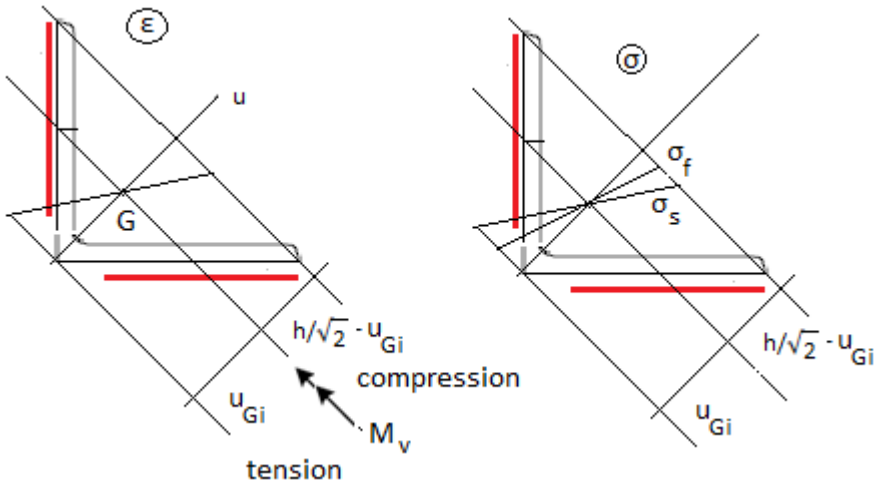

Figure 2.3: Strain and stress diagrams for elastic moment weak axis

$$\text{tip in compression } M_{v,el,i} = \min\left\{\frac{f_y \cdot I_{vi}}{u_{Gi}}, \frac{f_y \cdot I_{vi}}{h/\sqrt{2}-u_{Gi}}, \frac{f_{fc} \cdot I_{vi} \cdot n}{h/\sqrt{2}-u_{Gi}}\right\} \quad (2.8)$$

$$\text{tip in tension } M_{v,el,i} = \min\left\{\frac{f_y \cdot I_{vi}}{u_{Gi}}, \frac{f_y \cdot I_{vi}}{h/\sqrt{2}-u_{Gi}}, \frac{f_f \cdot I_{vi \cdot n}}{h/\sqrt{2}-u_{Gi}}\right\} \quad (2.9)$$

2.2.8 Elastic moment, strong axis

The elastic moment is determined from the condition that steel reaches its yield strength, since this obviously occurs before the FRP plates reach their strength.

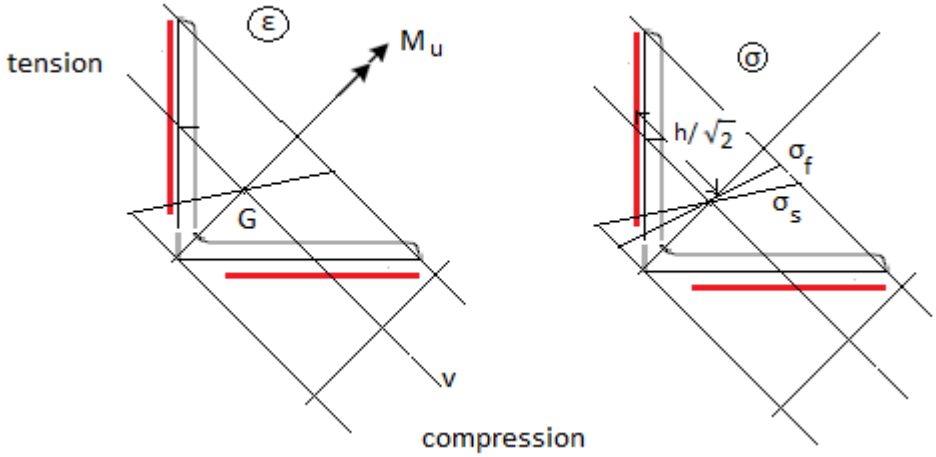

Figure 2.4: Strain and stress diagrams for elastic moment strong axis

$$M_{u,el,i} = \frac{f_y \cdot I_{ui}}{h/\sqrt{2}} \quad (2.10)$$

2.2.9 Limit elastic - plastic moment, weak axis

At the attainment of the ultimate limit moment it is supposed that the steel section is fully plastic, while the FRP plates elastic.

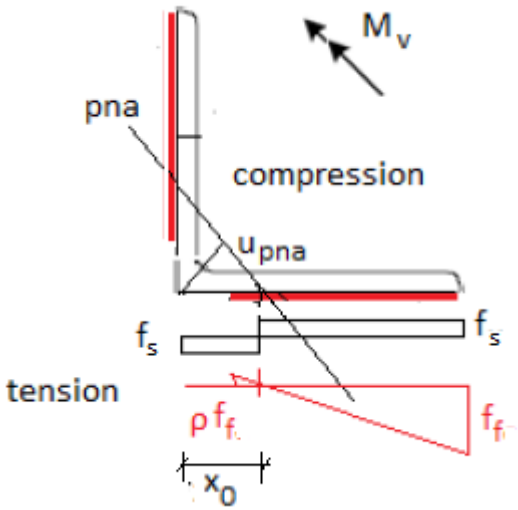

Figure 2.5: Stress diagram for limit elastic-plastic moment, weak axis

Stress ratio: $\rho = \frac{\chi_0 - (h-b)}{h - x_0}$ (2.11)

Compression/force $N_c = f_s \cdot t \cdot (h - x_0) + 0{,}5 f_f t_f \cdot (h - x_0)$ (2.12)

Tension/force $N_t = f_s \cdot t \cdot x_0 + 0{,}5 f_f t_f \cdot \frac{[\chi_0 - (h-b)]^2}{h - x_0}$ (2.13)

Determination of the position of the neutral axis from the condition:

$N_c = N_t$ (2.14)

Which is written as

$$ax_0^2 - bx_0 + c = 0 \quad (2.15)$$

where:

$$a = 2 f_s t \quad (2.16)$$

$$b = 3 f_s t h + f_f t_f b_f \quad (2.17)$$

$$c = f_s t h^2 - f_f t_f b_f \left(\frac{b_f}{2} - h\right) \quad (2.18)$$

Solving the above equation yields the position of the neutral axis:

$$x_0 = \frac{\frac{b}{2} - \sqrt{(b/2)^2 - ac}}{a} \quad (2.19)$$

The distance of the neutral axis from the angle heel is then equal to:

$$u_{pna} = \frac{x_0}{\sqrt{2}} \quad (2.20)$$

The elastic-plastic limit moment is finally determined from:

$$M_{v,el\text{-}pl} = \frac{f_s t}{\sqrt{2}} \cdot [(h - x_0)^2 + x_0^2] + \frac{2 f_f t_f}{3\sqrt{2}(h - x_0)} \{(h - x_0)^3 + [\chi_0 - (h - b)]^3\} \quad (2.21)$$

2.2.10 Limit elastic - plastic moment, strong axis

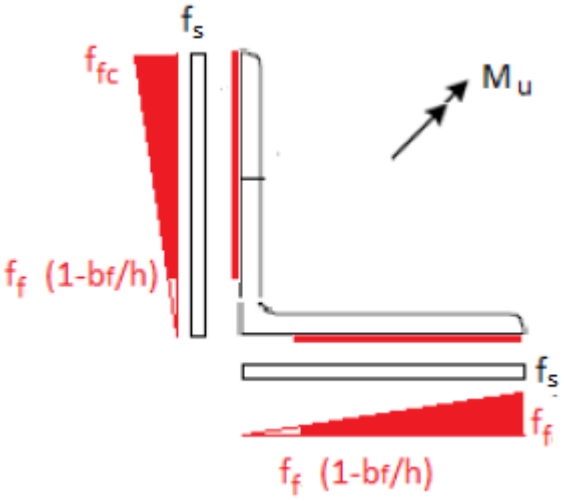

Figure 2.6: Stress diagram for limit elastic-plastic moment, strong axis

$$M_{u,el\text{-}pl} = M_{pl,s} + \frac{f_f t_f b(2b-h)}{3\sqrt{2}} \quad (2.22)$$

where

$M_{pl,s} = W_{pl} \cdot f_s$ plastic moment of the steel profile

W_{pl} plastic resistance moment of the steel profile

f_s limit strength for steel

2.3 Properties of the hybrid section composed of angle section steel + external and internal FRPs – principal axes

For reasons of simplicity the same formulae as in section 2.2 apply with doubling the thickness of the individual FRP plates t_f. Accordingly, in all formulae of section 2.2 f_f is substituted by $2f_f$.

2.4 Properties of the hybrid section composed of angle section steel + external FRPs – geometric axes

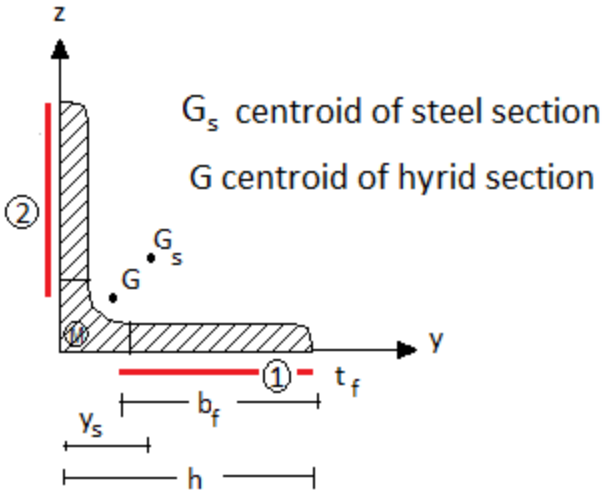

Figure 2.7: Notation and geometric axes for hybrid section

2.4.1 Cross-section area

Cross-section area of steel: A_s

Cross-section area of FRP: $A_f = 2 \cdot b_f \cdot t_f$ (2.23)

Cross-section area of equivalent section: $A_i = A_s + A_f/n$ (2.24)

2.4.2 Position of centroid:

Steel section: z_s

FRP sheet 1: $z_{f1} = h - b_f/2$ $z_{f1} = -z_s$

FRP sheet 2: $y_{f2} = -y_s$ $z_{f2} = h - b_f/2$

Equivalent section:

$$y_{Gi} = \frac{A_s \cdot y_s + A_f/2n \cdot (y_{f1} + y_{f2})}{A_i} \quad (2.25)$$

$$z_{Gi} = y_{Gi} \quad (2.26)$$

(alternatively: $y_{Gi} = z_{Gi} = \frac{A_s \cdot u_{Gs} + A_f/n \cdot u_{Gf}}{A_i\sqrt{2}}$)

2.4.3 Second moment of area,

$$I_{yi} = I_{ys} + A_s.(z_{Gi} - z_s)^2 + A_f/2n \cdot \left(z_{Gi} - z_{f1}\right)^2 + A_f/2n \cdot \left(z_{Gi} - z_{f2}\right)^2 \quad (2.27)$$

$$I_{zi} = I_{yi} \quad (2.28)$$

Remark: The FRP plates are considered to contribute only with the Steiner part.

2.4.4 Elastic moment, tip in tension, leg in compression

Since the steel stresses obviously attain their limit value before the FRP stresses, the elastic moment is determined considering the stress distribution at the steel profile.

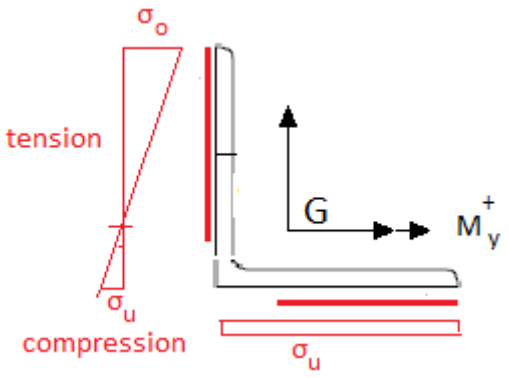

Figure 2.8: Stresses at the steel profile for moment on the geometric axis, leg in compression

$$\sigma_0 = \frac{M_y}{I_{yi}} \cdot (h - z_{Gi}) \le f_y \rightarrow \text{My,el} = \frac{f_y.I_{yi}}{(h - z_{Gi})} \text{ and } \quad \sigma_u = \frac{M_y}{I_{yi}} \cdot z_{Gi} \le f_y \rightarrow \text{My,el} = \frac{f_y.I_{yi}}{z_{Gi}}$$

$$\rightarrow \text{My,el} = min\left\{\frac{f_y.I_{yi}}{(h - z_{Gi})}, \frac{f_y.I_{yi}}{z_{Gi}}\right\} \quad (2.29)$$

2.4.5 Elastic moment, leg in tension

Here, the steel stresses attain their limit value before the FRP stresses, too.

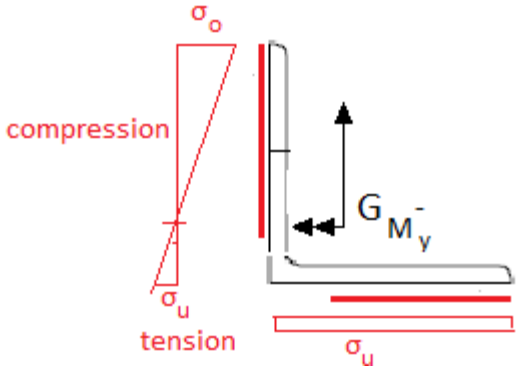

Figure 2.9: Stresses at the steel profile for moment on the geometric axis, leg in tension

$\sigma_0 = \frac{M_y}{I_{yi}} \cdot (h - z_{Gi}) \leq f_y \rightarrow$ My,el = $\frac{f_y \cdot I_{yi}}{(h - z_{Gi})}$ and $\sigma_u = \frac{M_y}{I_{yi}} \cdot z_{Gi} \leq f_y \rightarrow$ My,el = $\frac{f_y \cdot I_{yi}}{z_{Gi}}$

$\rightarrow$ My,el = $min\left\{\frac{f_y \cdot I_{yi}}{(h - z_{Gi})}, \frac{f_y \cdot I_{yi}}{z_{Gi}}\right\}$ (2.30)

2.4.6 Elastic-plastic moment, leg in compression

At the attainment of the ultimate limit moment it is supposed that the steel section is fully plastic, while the FRP plates elastic.

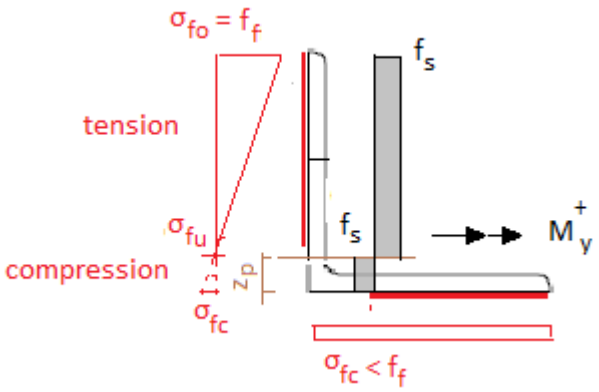

Figure 2.10: Stresses for elastic-plastic moment geometric axis, leg in compression

$\sigma_{fo} = f_f$ (2.31)

$\sigma_{fu} = f_f \cdot \frac{h - z_{p-b_f}}{h - z_p}$ (2.32)

$\sigma_{fc} = f_f \cdot \frac{z_p}{h - z_p}$ (2.33)

Tension force $N_t = f_s \cdot t \cdot (h - z_p) + \frac{\sigma_{fo} + \sigma_{fu}}{2} \cdot t_f \cdot b_f$ (2.34)

Compression force $N_c = f_s \cdot t \cdot (h + z_p) + f_f \cdot \frac{z_p}{h - z_p} \cdot t_f \cdot b_f$ (2.35)

$N_c = N_t \rightarrow$ Determination of position of neutral axis from relation

$a \cdot z_p^2 - 2b \cdot z_p - c = 0$ (2.36)

Where:

a = 2 f_y t b = f_s t h + f_f $b_f t_f$ c = - f_f b_f t_f (h - b_f/2)

position of neutral axis $z_p = \frac{b-\sqrt{b^2+ac}}{a} > t + r$ (2.37)

$M_{u,y} = f_s \cdot t \cdot (h + z_p) \cdot \left(z_p - \frac{t}{2}\right) + \sigma_{fc} \cdot t_f \cdot b_f \cdot z_p + 0.5 \cdot f_s \cdot t \cdot (h - z_p)^2 + \frac{\sigma_{fo}+\sigma_{fu}}{2} \cdot t_f \cdot (h - b_f) \cdot \frac{2}{3}\left(\frac{5}{3} b_f - z_p\right)$ (2.38)

2.4.7 Elastic-plastic moment, leg in tension

At the attainment of the ultimate limit moment it is supposed that the steel section is fully plastic, while the FRP plates elastic.

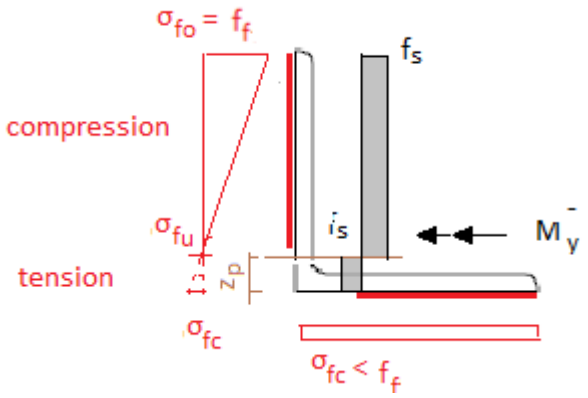

Figure 2.11: Stresses for elastic-plastic moment geometric axis, leg in tension

$\sigma_{fo} = f_f$ (2.39)

$\sigma_{fu} = f_f \cdot \frac{h - z_p - b_f}{h - z_p}$ (2.40)

$\sigma_{fc} = f_f \cdot \frac{z_p}{h - z_p}$ (2.41)

Tension force $N_t = f_s \cdot t \cdot (h - z_p) + \frac{\sigma_{fo}+\sigma_{fu}}{2} \cdot t_f \cdot b_f$ (2.42)

Compression force $N_c = f_s \cdot t \cdot (h + z_p) + \sigma_{fc} \cdot t_f \cdot b_f$ (2.43)

$N_c = N_t \rightarrow$ Determination of position of neutral axis from relation

$a \cdot z_p^2 - 2b \cdot z_p - c = 0$ (2.44)

Where:

$a = 2\, f_s\, t \quad b = f_s\, t\, h + f_f\, b_f\, t_f \quad c = -\, f_f\, b_f\, t_f\, (h - b_f/2)$

position of neutral axis $z_p = \frac{b-\sqrt{b^2+ac}}{a} > t + r$ (2.45)

$$M_{u,y} = f_s \cdot t \cdot (h + z_p) \cdot \left(z_p - \frac{t}{2}\right) + \sigma_f \cdot t_f \cdot b_f \cdot z_p + 0.5 \cdot f_s \cdot t \cdot (h - z_p)^2 + \frac{\sigma_{fo}+\sigma_{fu}}{2} \cdot t_f \cdot (h - b_f) \cdot \frac{2}{3}\left(\frac{5}{3} b_f - z_p\right) \quad (2.46)$$

3 Safety factors

3.1 General

Scientific literature concerning structural strengthening using fibre composite materials is widely spread worldwide for concrete structures. Some assumptions on safety factors for composite materials have been made and depend on design guidelines. These safety factors are commonly inherent to the materials. Design guidelines used in Europe are the followings:

- Technical Report n°55, Third Edition (2012): Design guidance for strengthening concrete structures using fibre composite materials, based on Eurocode 2, part 1-1 (England).
- AFGC 2011: Réparation et Renforcement des Structures en béton au moyen des Matériaux Composites, based on Eurocode 2, part 1-1 (France).
- CNR-DT 200 R1/2013: Istruzioni per la Progettazione, l'Esecuzione ed il Controllo di Interventi di Consolidamento Statico mediante l'utilizzo di Compositi Fibrorinforzati (Italy).
- Fib 14 (2001) : Design and use of externally bonded fibre reinforced polymer reinforcement (FRP EBR) for reinforced concrete structures, based on Eurocode 2, part 1-1 (Switzerland).

Nevertheless, regarding steel structures, complementary safety factors should be taken into account because of environmental, fatigue or long-term effects. Only few guidelines present these assumptions such the Italian ones CNR-DT 202 2005 [6].

3.2 Partial factors

Partial factors for steel (according to EN 1993-1-1):

- $\gamma_{M0} = 1.0$
- $\gamma_{M1} = 1.0$

Partial factors of the FRP strengthening γ_f:

- Type A application = 1.10
- Type B application =1.25

Table 3.1: Different types of application

Type A application	Strengthening system with certification of each component as well as the final product to be applied to a given support.
Type B application	Strengthening systems certified for each component only.

Partial factor for the adhesive interface γ_a:

- Type A application = 1.20
- Type B application = 1.50

Partial factors for resistance models (ULS) γ_{Rd}:

- Bending/Combined bending and axial load = 1.00
- Shear/Torsion = 1.00
- Delamination = 1.20
- Fatigue = 1.20

3.3 Conversion factor

Conversion factor $\eta = \eta_a \cdot \eta_1$

Environmental reduction factor for CFRP η_a:

- Internal exposure = 0.95
- External exposure = 0.85
- Aggressive environment = 0.85

Reduction factor for long term effects for CFRP η_1:

- Continuous (creep and relaxation) = 0.80
- Cyclic (fatigue) = 0.50

For metallic structures strengthened with FRPs following environmental and time partial factors are proposed by Cadei et al [8]:

Environmental factor γ_{me}:

- Adhesive properties determined for the environmental conditions in service = 1.0
- Adhesive properties determined for environmental conditions different from service conditions = 2.0

Time-related factor γ_{mt}:

- Long-term loading = 2.0
- Short-term loading = 1.0

For bridges following values of partial factors for carbon FRP materials for the ultimate limit state are proposed in the Design Manual for Roads and Bridges [9]:

Material partial safety factor for FRP stiffness:

- γ_{mfE} = 1.15

Material partial safety factor for FRP strain:

- $\gamma_{mf\varepsilon}$ = 1.15 (for Combination 4 loadings in accordance with BD 37, DMRB 1.3.14)
- $\gamma_{mf\varepsilon}$ = 1.47 (excluding Combination 4 loadings in accordance with BD 37, DMRB 1.3.14)

Material partial safety factor for the adhesive:

- γ_{ma} = 5

These safety factors shall be applied to the characteristic values of the material properties.

According to this design manual, no environmental factors are taken into account.

4 Cross-section design

4.1 Cross-section classification

The design rules refer to cross-sections that attain at the limit the elastic-plastic moment as derived in the previous section 2.

4.2 Design resistance to axial force

4.2.1 Compression

$$N_{c,Rd} = A_s \cdot \frac{f_y}{\gamma_{M1}} + A_f \cdot \frac{\eta \cdot k \cdot f_f}{\gamma_f} \quad (4.1)$$

The reduction factor of the FRP strength for compression is k = 0,5.

4.2.2 Tension

$$N_t = A_s \cdot \frac{f_y}{\gamma_{M0}} + A_f \cdot \frac{\eta \cdot f_f}{\gamma_f} \quad (4.2)$$

4.3 Design resistance to strong axis bending

Elastic-plastic design moment:

$$M_{u,el\text{-}pl,Rd} = M_{pl,s,Rd} + \frac{\eta \cdot f_f \cdot t_f \cdot b \cdot (2b-h)}{3\sqrt{2} \cdot \gamma_f} \quad (4.3)$$

4.4 Design resistance to weak axis bending

Elastic-plastic design moment:

$$M_{v,pl,Rd} = \frac{f_y \cdot t}{\sqrt{2} \cdot \gamma_{M0}} \cdot \{(h - x_0)^2 + x_0^2\} + \frac{2 \cdot \eta \cdot f_f \cdot t_f}{3 \cdot \sqrt{2} \cdot (h - x_0) \cdot \gamma_f} \{(h - x_0)^3 + [x_0 - (h - b)]^3\} \quad (4.4)$$

4.5 Design resistance to combined effects

For compression axial force and biaxial moments, the same interaction relation developed during the current research project and included in Deliverable 2.2 for steel angle profiles is adopted [10].

The interaction relation for tension and biaxial moment is linear, while for compression and biaxial moment non-linear.

Tension force

$$\frac{N_{Ed}}{N_{t,Rd}} + \frac{M_{u,Ed}}{M_{u,el-pl,Rd}} + \frac{M_{v,Ed}}{M_{v,el-pl,Rd}} \leq 1.0 \quad (4.5)$$

Compression force

$$\left(\frac{N_{Ed}}{N_{c,Rd}} + \frac{M_{u,Ed}}{M_{u,el-pl,Rd}}\right)^{\xi} + \frac{M_{v,Ed}}{M_{v,el-pl,Rd}} \leq 1 \quad (4.6)$$

where:

N_{Ed} design axial compression force, absolute value

$M_{u,Ed}$ design strong axis moment, absolute value

$M_{v,Ed}$ design weak axis moment, absolute value

$\xi = 2$ (4.7)

5 Member design

5.1 Compression

Design axial force capacities

$$N_{bu,Rd} = \chi_u \cdot N_{c,Rd} \quad (5.1)$$

$$N_{bv,Rd} = \chi_v \cdot N_{c,Rd} \quad (5.2)$$

$$N_{b,Rd} = \min\{N_{bu,Rd}, N_{bv,Rd}\} \quad (5.3)$$

Slenderness

$$\bar{\lambda}_u = \sqrt{\frac{N_{c,R}}{N_{cr,u}}} \quad (5.4)$$

$$\bar{\lambda}_v = \sqrt{\frac{N_{c,R}}{N_{cr,v}}} \quad (5.5)$$

Critical buckling loads

$$N_{cr,u} = \frac{\pi^2 \cdot E_s \cdot I_{ui}}{l^2} \quad (5.6)$$

$$N_{cr,v} = \frac{\pi^2 \cdot E_s \cdot I_{vi}}{l^2} \quad (5.7)$$

Reduction factors χ_u, χ_v as functions of the slenderness derived from buckling curve **b**

$\chi_{min} = \min\{\chi_u, \chi_v\}$ (5.8)

5.2 Strong axis bending

$$M_{b,Rd} = \chi_{LT} \cdot M_{u,el-pl,Rd} \quad (5.9)$$

- Determination of χ_{LT}

Critical LTB moment: $M_{cr} = C_b \frac{0{,}46 \cdot E \cdot h^2 \cdot \left(t + t_f/n\right)^2}{l}$ (5.10)

Table 5.1: C_b factor for the determination of the critical LTB moment

$C_b = \frac{12.5M_{max}}{2.5M_{max} + 3M_A + 4M_B + 3M_C} \leq 1.5$ For linear moment distribution with -1 ≤ψ=$\frac{M_2}{M_1}$≤1 $C_b = \frac{12,5}{7,5+5\psi}$	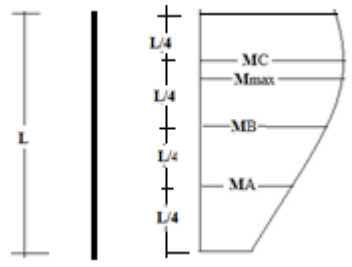

Slenderness to LTB $\bar{\lambda}_{LT} = \sqrt{\frac{M_{u,el-pl}}{M_{cr}}}$ (5.11)

Reduction factor χ_{LT} as function of the LTB slenderness derived from buckling curve **d**

Based on EN 1993-1-1, lateral torsional buckling effects need not be considered and χ_{LT} is set to $\chi_{LT} = 1$ when one of the following conditions apply:

- $\bar{\lambda}_{LT} \leq \bar{\lambda}_{LT,0}$ with $\bar{\lambda}_{LT,0}$=0,4 (5.12a)
- $\frac{M_{Ed}}{M_{cr}} \leq \bar{\lambda}_{LT,0}^{\ 2}$ (5.12b)
- $\frac{N_{Ed}}{N_{bu,Rd}} > 0{,}5$ (5.13a)
- $\frac{N_{Ed}}{N_{bv,Rd}} > 0{,}5$ (5.13b)

5.3 Weak axis bending

$M_{v,el-pl,Rd}$

5.4 Combined effects – Compression and bending

- **Strong axis check**

$$\left(\frac{N_{Ed}}{N_{bu,Rd}} + k_{uu}\frac{M_{u,Ed}}{M_{b,el-pl,Rd}}\right)^{\xi} + k_{uv}\frac{M_{v,Ed}}{M_{v,el-pl,Rd}} \leq 1 \quad (5.14)$$

- **Weak axis check**

$$\left(\frac{N_{Ed}}{N_{bv,Rd}} + k_{vu}\frac{M_{u,Ed}}{M_{b,el-pl,Rd}}\right)^{\xi} + k_{vv}\frac{M_{v,Ed}}{M_{v,el-pl,Rd}} \leq 1 \quad (5.15)$$

Factors

$$k_{uu} = \frac{C_u}{1-\frac{N_{Ed}}{N_{cr,u}}} \quad (5.16)$$

$$k_{uv} = C_v \quad (5.17)$$

$$k_{vu} = C_u \quad (5.18)$$

$$k_{vv} = \frac{C_v}{1-\frac{N_{Ed}}{N_{cr,v}}} \quad (5.19)$$

$C_u = 0{,}6+0{,}4\psi_u \quad -1 \leq \psi_u = \frac{M_{2u}}{M_{1u}} \leq 1$ (5.20)

$C_v = 0{,}6+0{,}4\psi_v \quad -1 \leq \psi_v = \frac{M_{2v}}{M_{1v}} \leq 1$ (5.21)

$\xi = 2$ (5.22)

6 Experimental validation

6.1 Cross section properties

6.1.1 Second moment of area, moment capacity

The analytical expressions for the stiffness, the position of the neutral axis and the design moment are validated by comparison with the results of the experimental tests. More specifically, the experimental load – deflection curves are compared to the analytical ones. The analytical curves are considered as bilinear, composed from the elastic part and cut-off by the load at achievement of the elastic-plastic moment.

The elastic part is determined by the load – deflection relation of a simply supported beam loaded by a point load at mid-span. The mid-span deflection is written as:

$$\delta = \frac{P \cdot l^3}{48 E_s I} \tag{6.1}$$

where:

δ is the deflection at mid-span

l is the span

E_s is the modulus of elasticity for steel

I is the second moment of area of the hybrid cross section as derived in section 2

The cut-off limit is determined from:

$$P_u = \frac{4 \cdot M_{el-pl}}{l} \tag{6.2}$$

Where:

$M_{el\text{-}pl}$ is the elastic-plastic moment of the hybrid cross section as presented in section 2.

The experimental and analytical curves from the bending tests are given below. The elastic-plastic moment is calculated with two alternative limit stresses:

a) Setting the limit stress for steel $f_s = f_y$ and for FRP $f_f = k \cdot f_{fnom}$

where k is the experimentally determined reduction factor given by the relation:

$$k = \frac{E_f \cdot \varepsilon_{u,FRP}}{f_{f,nom}} \tag{6.3}$$

E_f is the modulus of elasticity of the FRP

$\varepsilon_{u,FRP}$ is the strain measured on the FRP during the bending tests at the attainment of the limit load

$f_{f,nom}$ is the nominal tensile strength of the FRP material

b) Setting the limit stress for steel $f_s = (f_y + f_u)/2$ and for FRP $f_f = f_{fnom}$

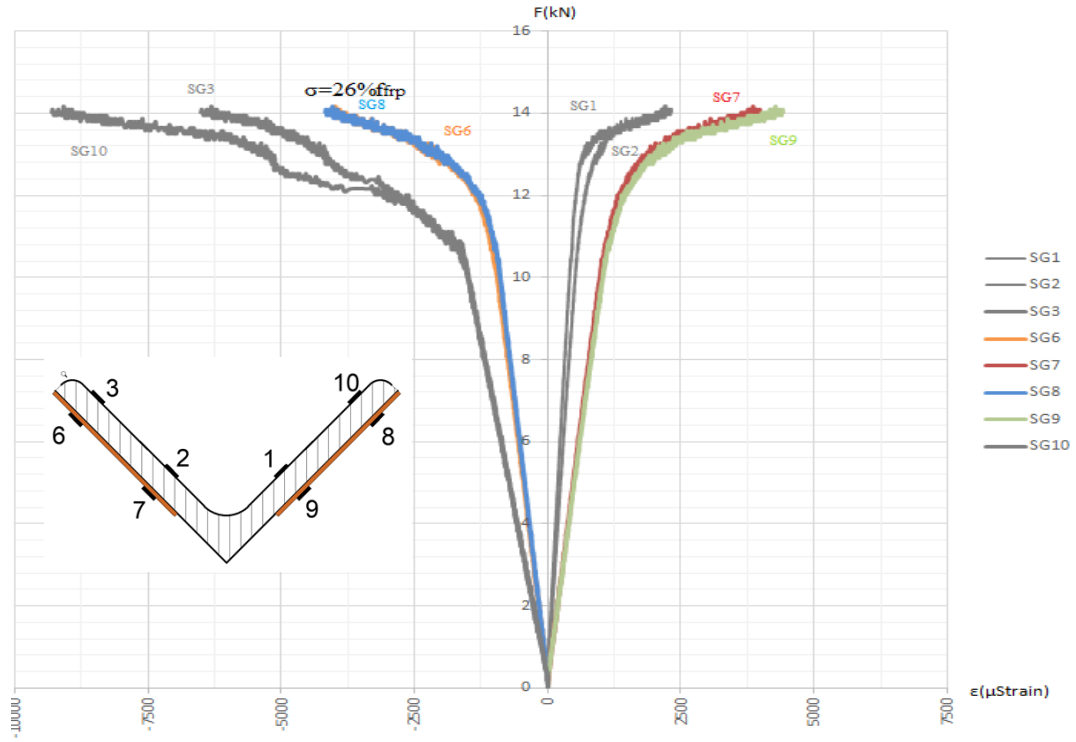

Figure 6.1: Limit FRP strain at maximal load, specimen B-T1-V

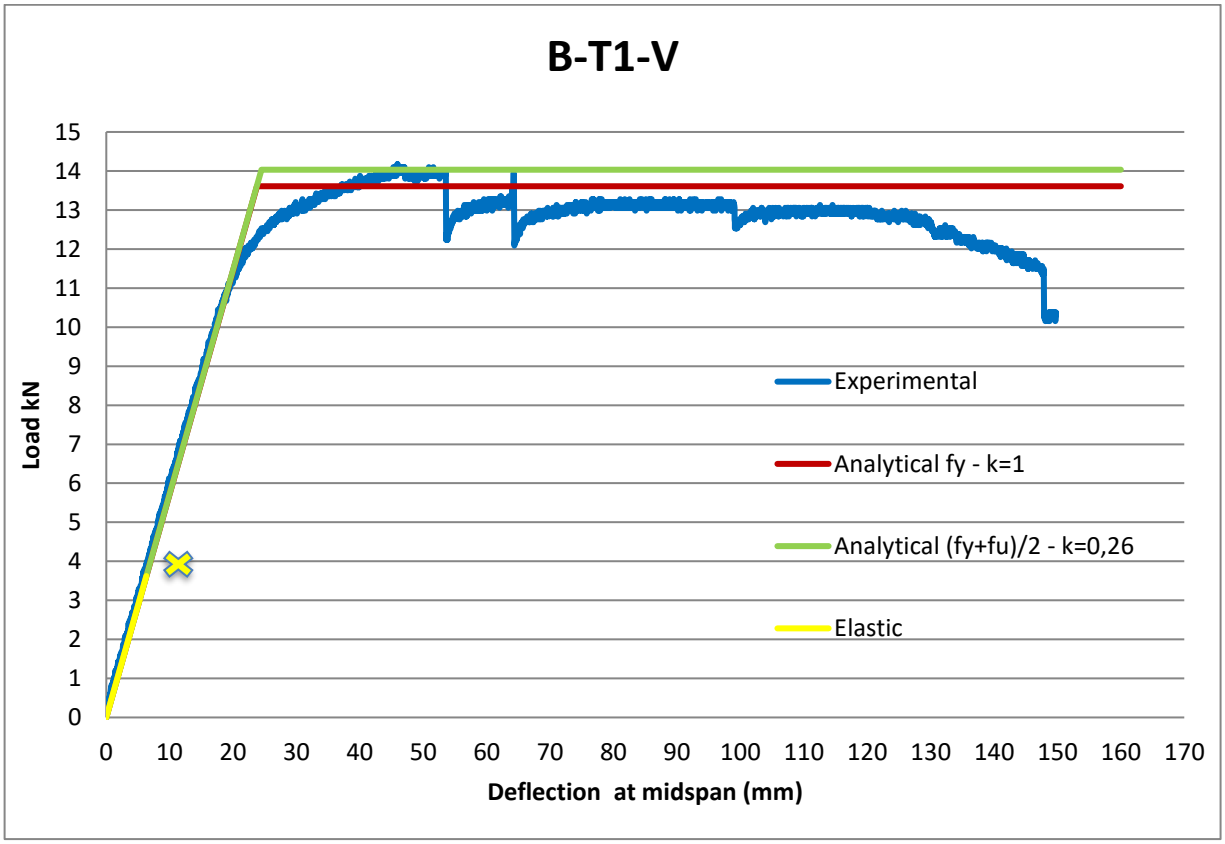

Figure 6.2: Experimental vs analytical load –deflection curves for bending on the weak axis, hybrid section with external FRP

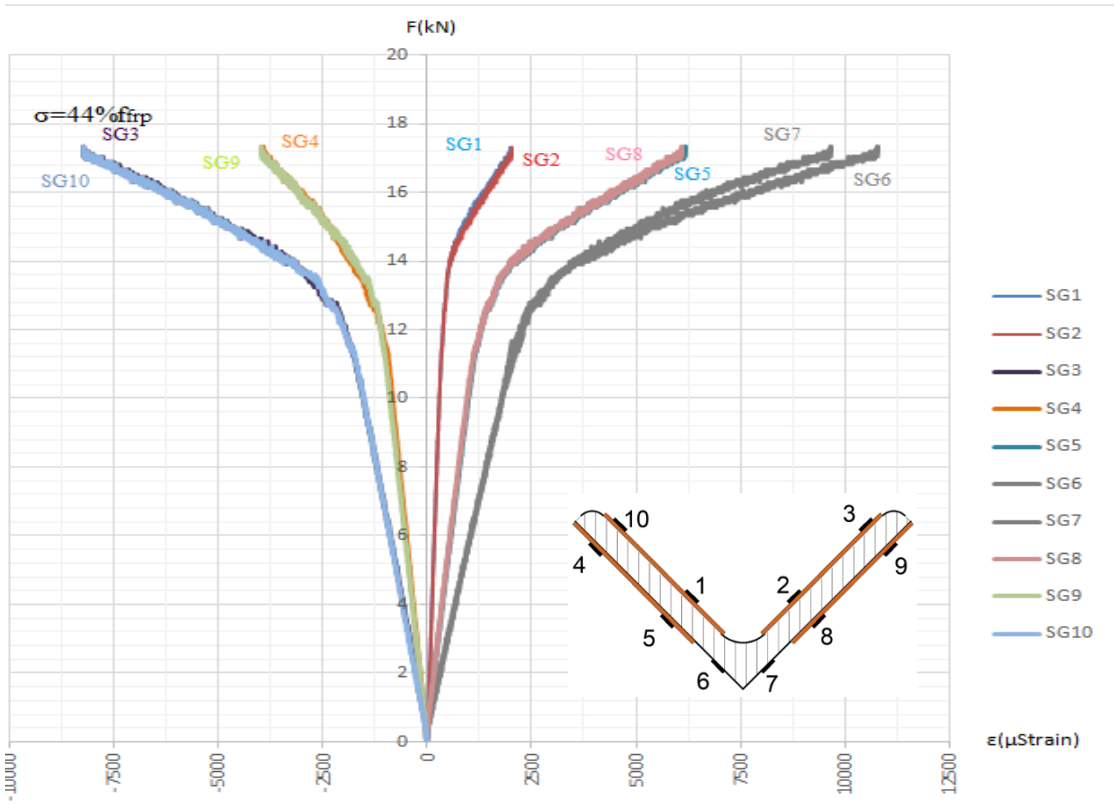

Figure 6.3: Limit FRP strain at maximal load, specimen B-T2-V2

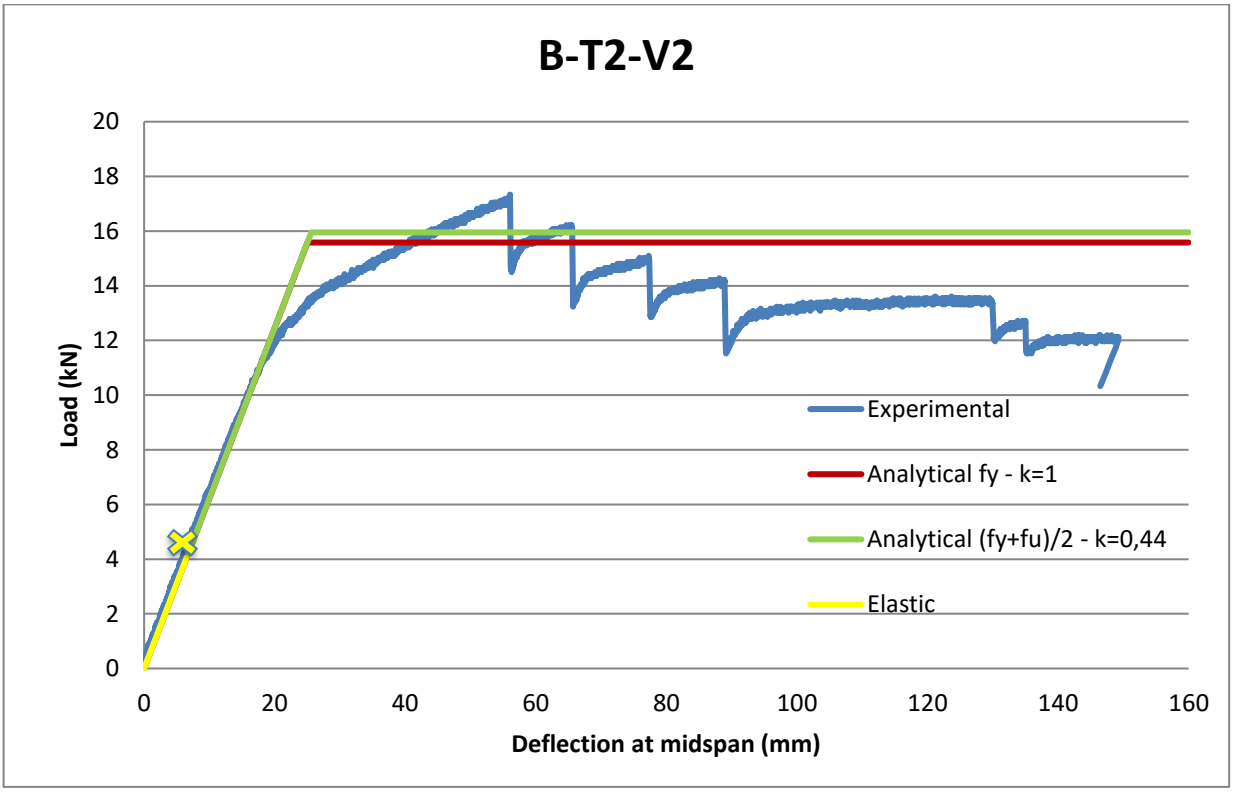

Figure 6.4: Experimental vs analytical load –deflection curves for bending on the weak axis, hybrid section with external + internal FRP

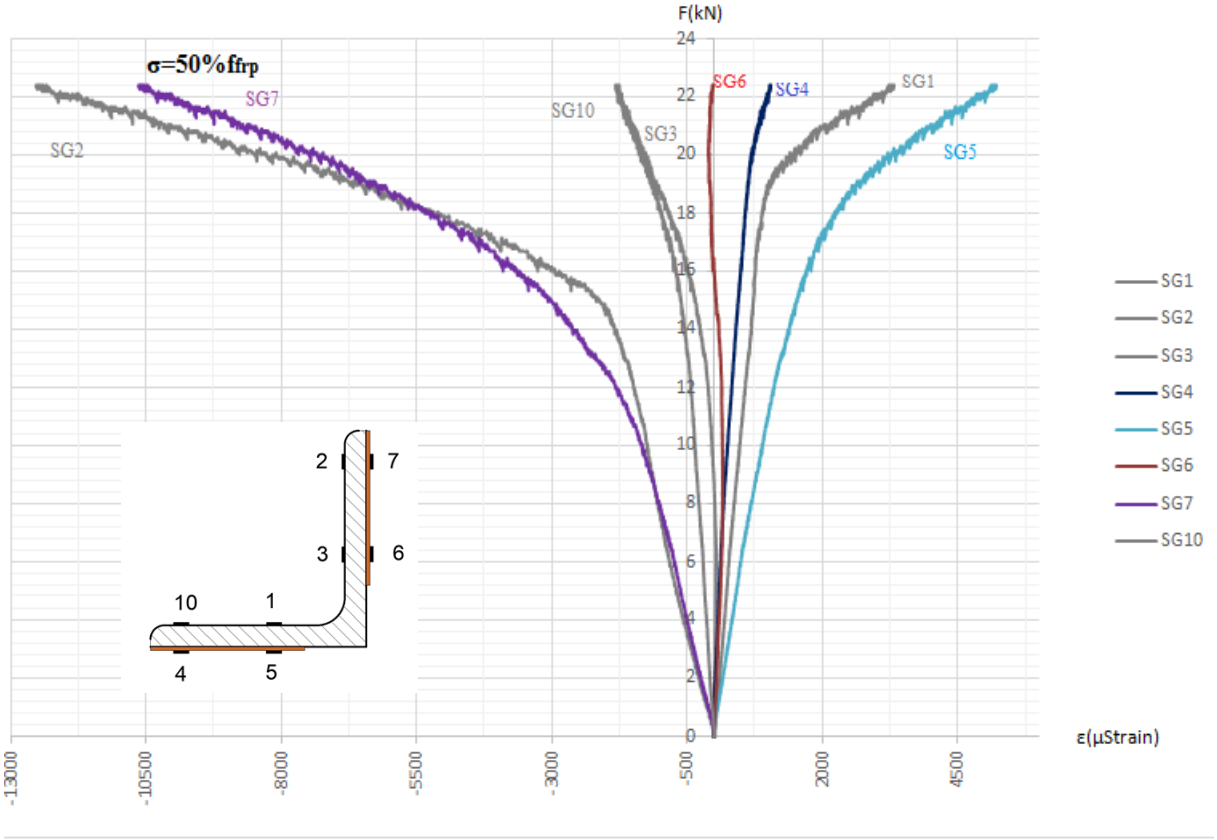

Figure 6.5: Limit FRP strain at maximal load, specimen B-T1-L

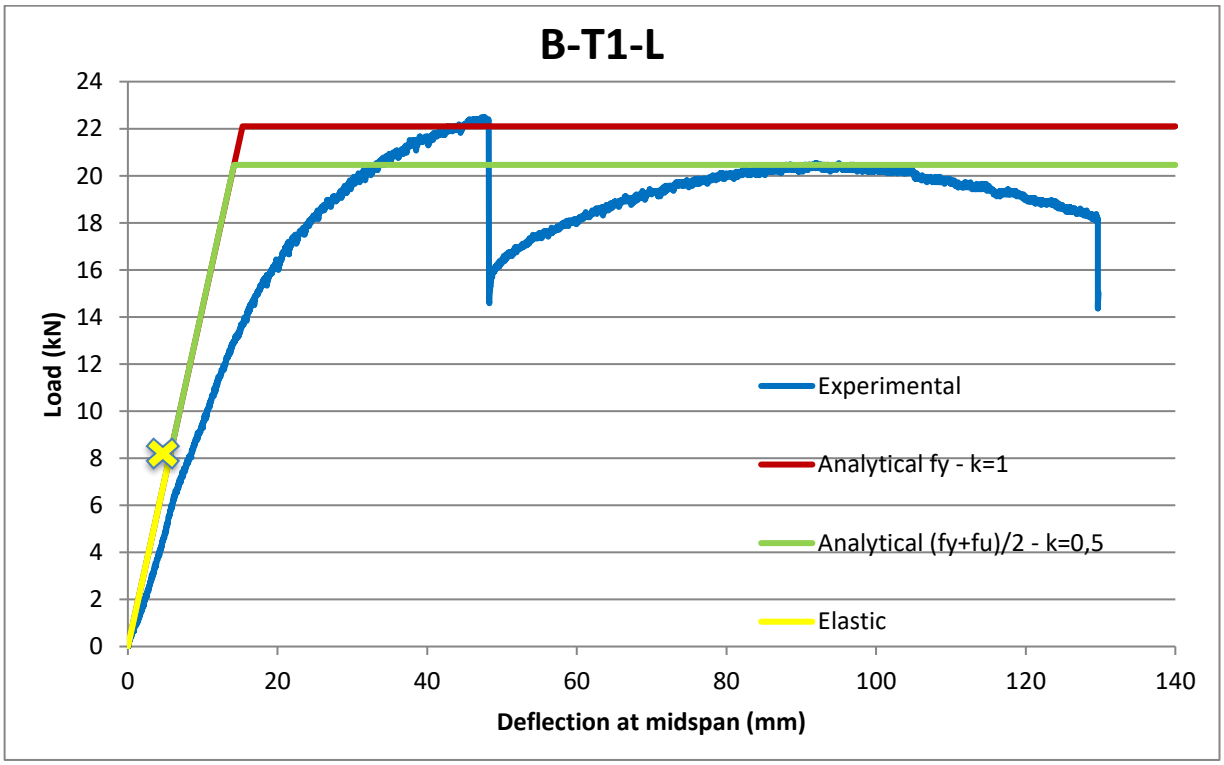

Figure 6.6: Experimental vs analytical load –deflection curves for bending on the geometric axis. Leg in tension. Hybrid section with external FRP

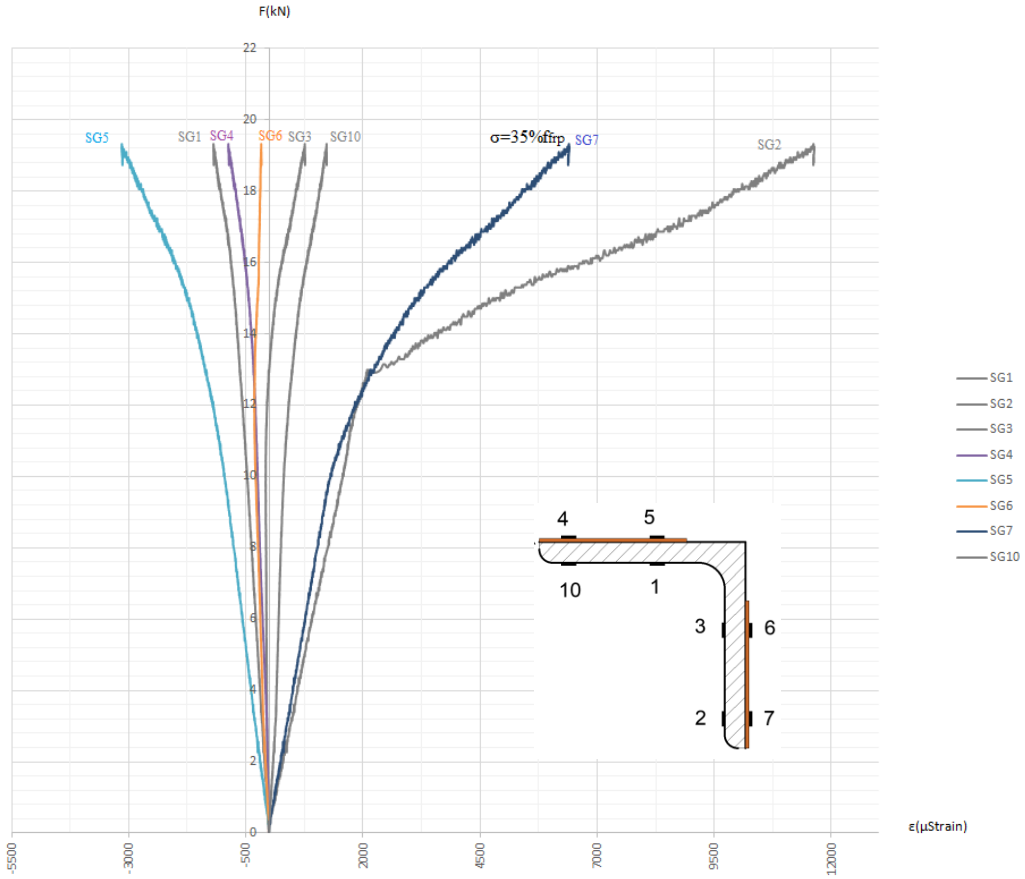

Figure 6.7: Limit FRP strain at maximal load, specimen B-T1-L1

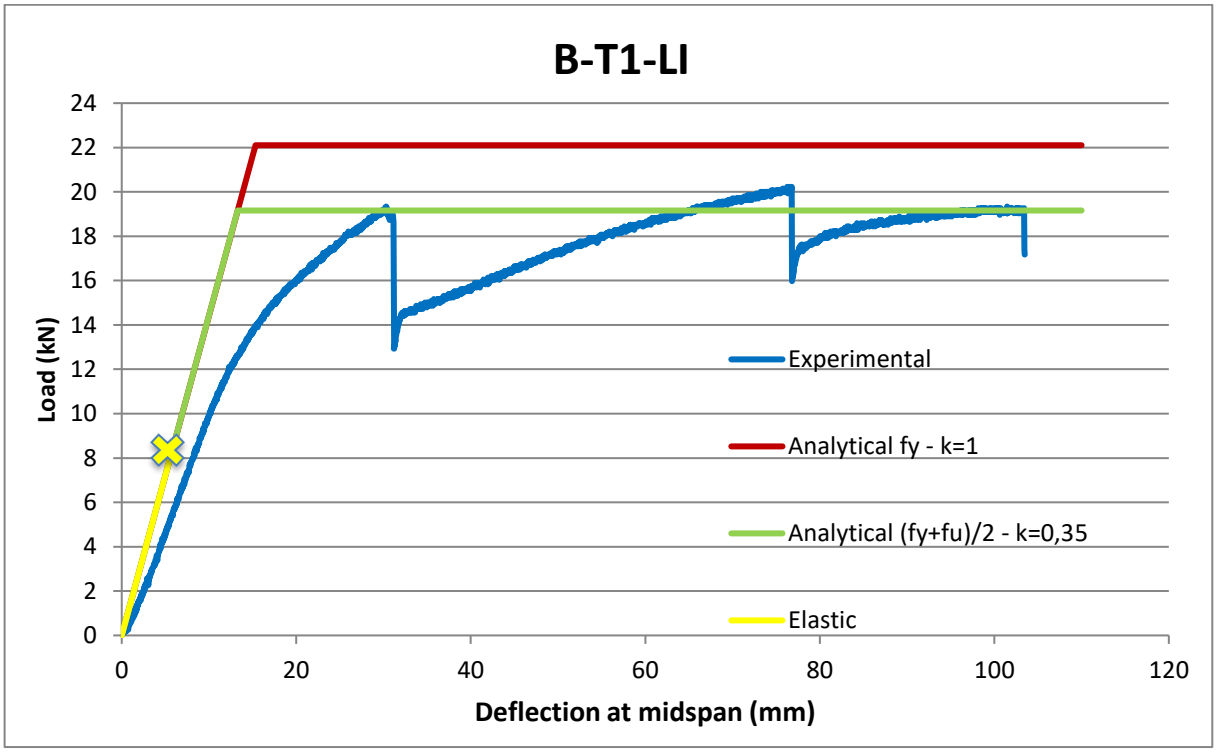

Figure 6.8: Experimental vs analytical load –deflection curves for bending on the geometric axis. Leg in compression. Hybrid section with external FRP

The comparison between experimental and analytical curves indicates the following:

- The analytically derived elastic lines compare well with the correspondent experimental curves. The two curves practically coincide for bending around the principal weak axis for the cases of FRP-strengthening in both the external and external + internal side of the legs. Small deviation for bending around the geometric axis is possibly due to small twist of the beam. Consequently, the expressions for the second moment of area for the hybrid section proposed in section 2 are good estimates and may be used in analysis of hybrid cross-sections.
- The limit loads based on the analytically derived elastic-plastic moments of the hybrid cross-sections compare well with the experimentally achieved limit loads. This is valid both pair of limit stresses for steel and FRP. It may be seen that the steel section is subject to strain hardening at limit load which counterbalances the premature de-bonding of the FRP prior to the attainment of its nominal tensile strength. For the sake of simplicity, it is then proposed to determine the elastic-plastic moment resistance of the hybrid section on the basis of the yield stress of steel, ignoring thus strain hardening, and the nominal FRP strength, ignoring thus de-bonding.
- Elastic analysis is overconservative in the prediction of the limit load.

6.1.2 Position of the centroid

Further on, the expressions proposed in section 2 for the position of the centroid and the elastic neutral axis were validated by comparison with the strain measurements during the tests. As written in the relevant report, strain measurements were made during the tests at different points of the cross-section at mid-span. The experimental values may be compared to the corresponding analytical values during elastic behavior and the position of the neutral axis from the tests derived. Indeed, the strain at any point of the cross section for a given moment in the elastic range may be determined by following expression:

$$\varepsilon = \frac{M}{EI} \cdot e \tag{6.4}$$

Where:

M is the applied moment

I is the second moment of area of the hybrid cross-section

E is the modulus of elasticity of steel or FRP, depending on where the strain is measured

e is the distance of the specific point from the cross-section centroid

By solving in respect to e, the above expression allows the back-calculation of the position of the centroid from the measurements of the strains during the tests. This was done for a moment M within the elastic range and the relevant results compared with the centroid's position as derived analytically. The correspondent results are illustrated in the next figures. As expected, the strain measurements do not provide a fixed point as a centroid. This is most probably due to the fact that the accuracy of the estimate of the actual position of the strain gage (SG) in the specimen's cross-section was not as high. This holds especially for the strain gages attached to the FRP's, where the thickness of the glue had to be estimated. However, it may be seen that the experimental results do not deviate strongly from the analytically derived position, especially for bending around the weak axis.

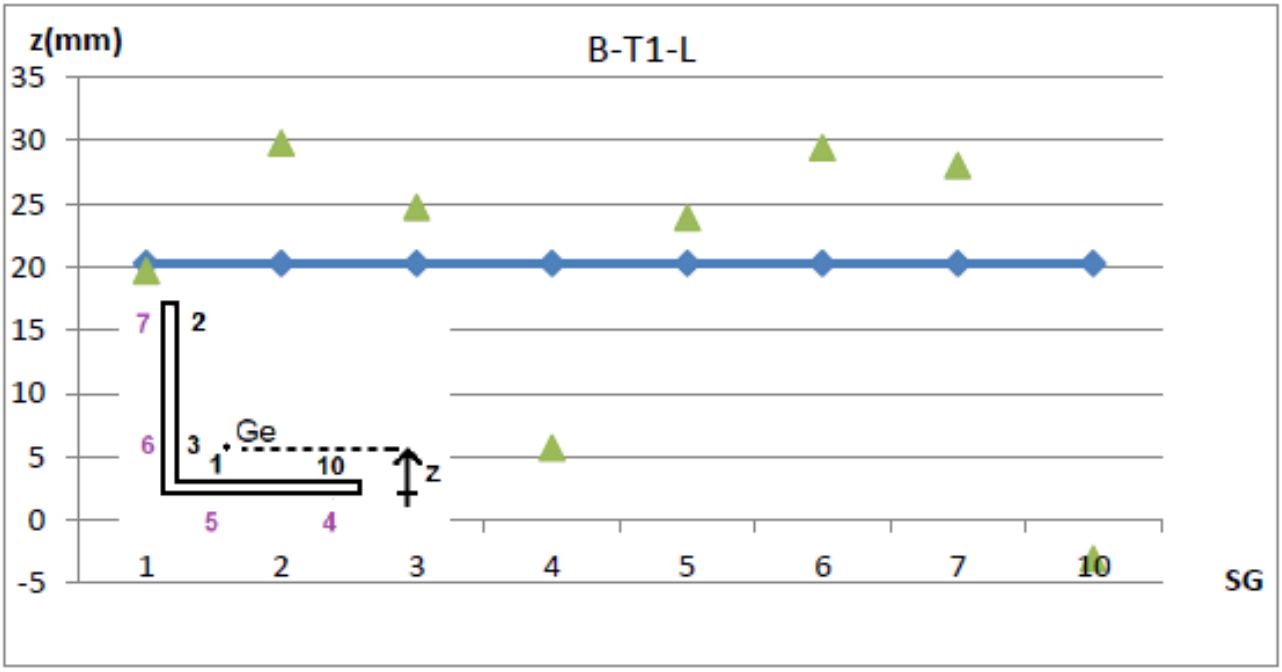

Figure 6.9: Position of the cross-section centroid. Analytical (blue) vs experimental from strain measurements (green). Bending around the geometric axis, leg in tension. SG in black are attached to steel, SG in magenta are attached to FRP

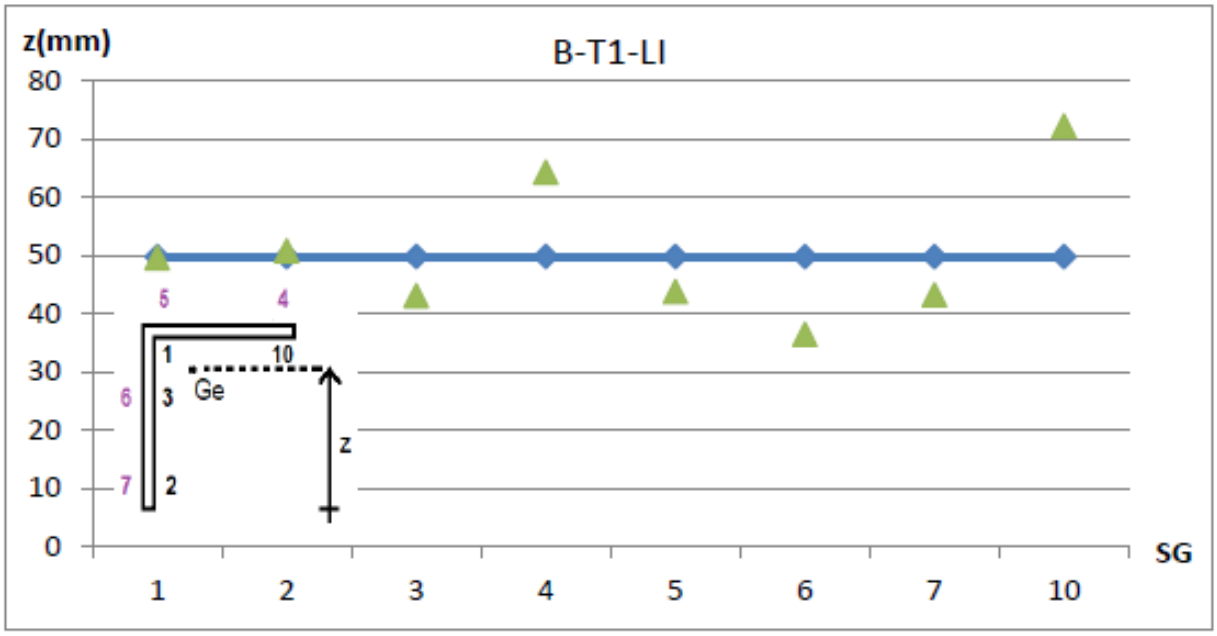

Figure 6.10: Position of the cross-section centroid. Analytical (blue) vs experimental from strain measurements (green). Bending around the geometric axis, leg in compression. SG in black are attached to steel, SG in magenta are attached to FRP

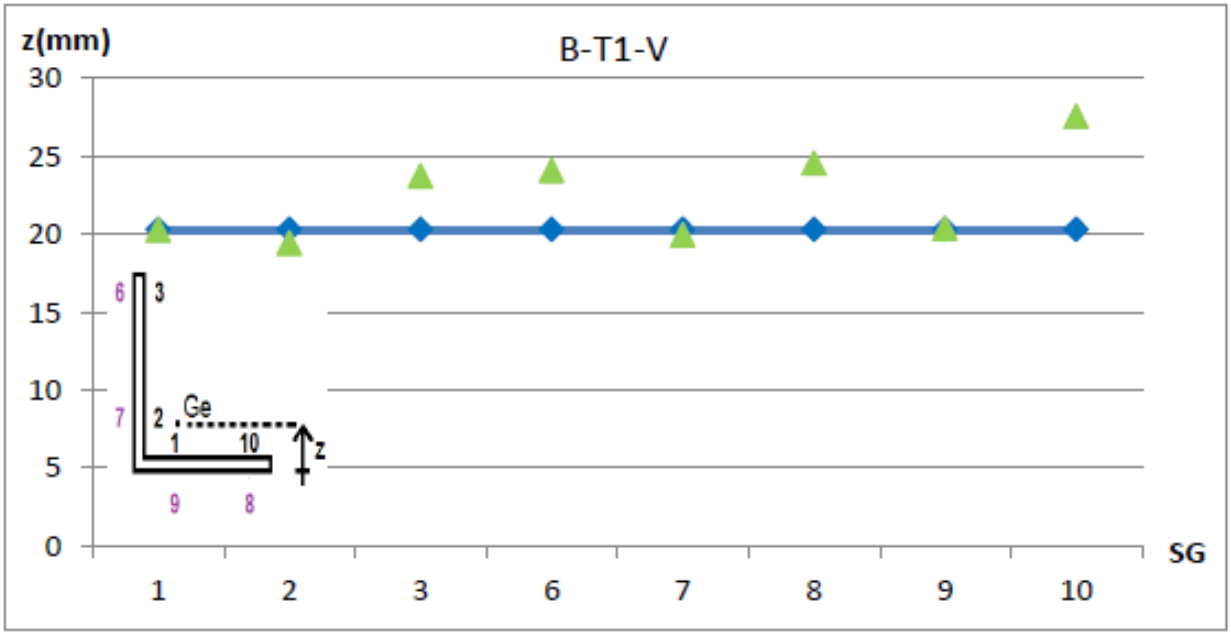

Figure 6.11: Position of the cross-section centroid. Analytical (blue) vs experimental from strain measurements (green). Bending around the weak axis, external FRP. SG in black are attached to steel, SG in magenta are attached to FRP

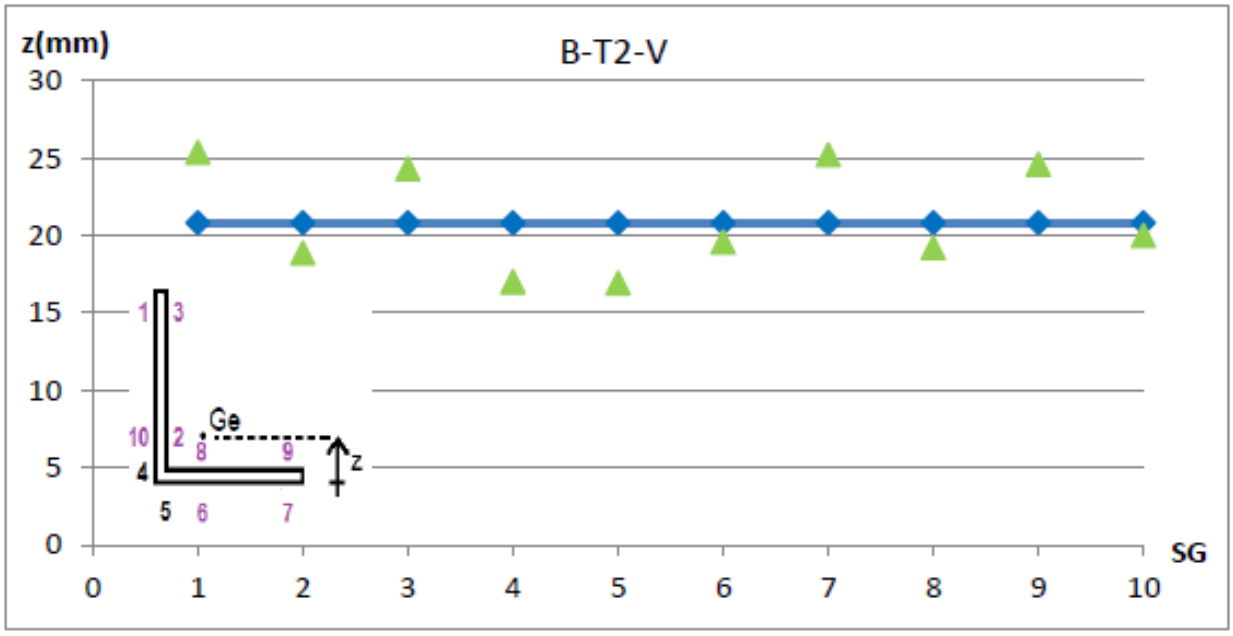

Figure 6.12: Position of the cross-section centroid. Analytical (blue) vs experimental from strain measurements (green). Bending around the weak axis, eternal + internal FRP. SG in black are attached to steel, SG in magenta are attached to FRP

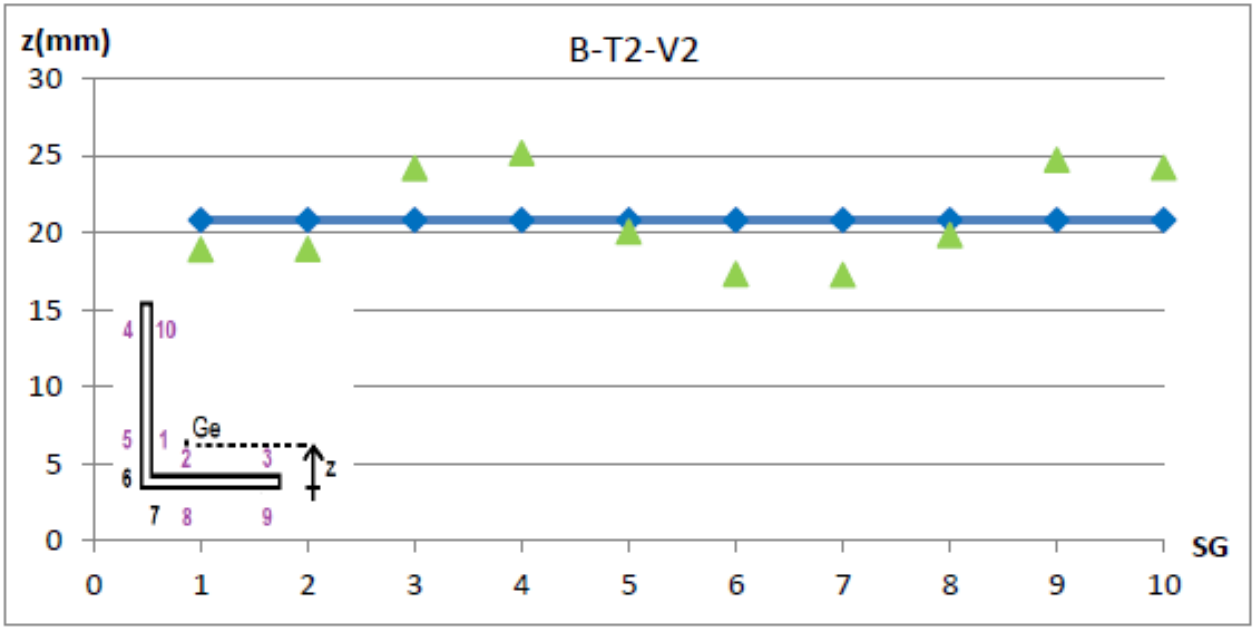

Figure 6.13: Position of the cross-section centroid. Analytical (blue) vs experimental from strain measurements (green). Bending around the weak axis, eternal + internal FRP. SG in black are attached to steel, SG in magenta are attached to FRP

It may be generally concluded that the analytical expressions for the cross-section properties as proposed in chapter 2 are valuable estimates of the actual properties.

6.2 Design interaction formulae

The proposed formulae for member design are validated by comparison with the results of the buckling tests performed at NTUA and reported in the relevant report of task 2.3. The tests referred to L70.70.7 angle profiles strengthened with FRP plates of dimensions 50x1.2 mm, applied on the external side of the legs, or on both external and internal side of them. Fig. 6.14 presents the ratio between the experimental and the theoretical compression force as derived from application of the proposed design formulae for the specimens with external FRPs, while Fig. 6.15 the correspondent curve for those with external and internal FRPs. In addition, the figures present the mean value and the mean value minus one standard deviation line of the ratio for all specimens.

For the specimens with external FRPs following observation can be made:

1. All tests but two achieved higher experimental forces than those predicted by the analytical formulae.
2. The specimens with no eccentricity subjected to pure compression exhibit considerably higher resistance than the predicted by the design formulae.one
3. The specimens subjected to compression and weak axis bending exhibit resistance close to the one predicted by the design formulae.
4. The specimens subjected to compression and strong axis bending exhibit resistance considerably higher to the one predicted by the design formulae. This holds for all tests but one, where lower resistance was achieved due to premature delamination of the FRP plates that extended over a partial length.
5. The statistical evaluation shows that the design formulae provide overall safe results with mean minus one standard deviation value for all tests a little higher than one.

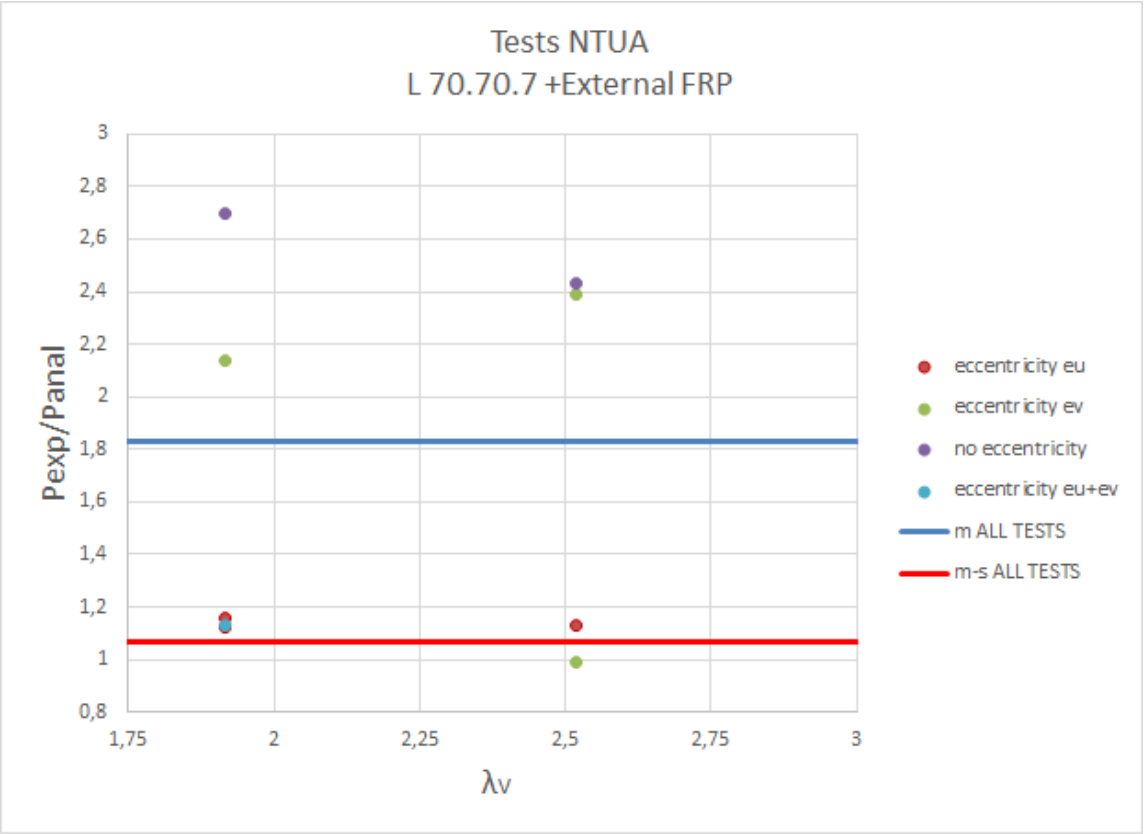

Figure 6.14: Ratio between experimental and analytical ultimate load. Specimens with external FRPs

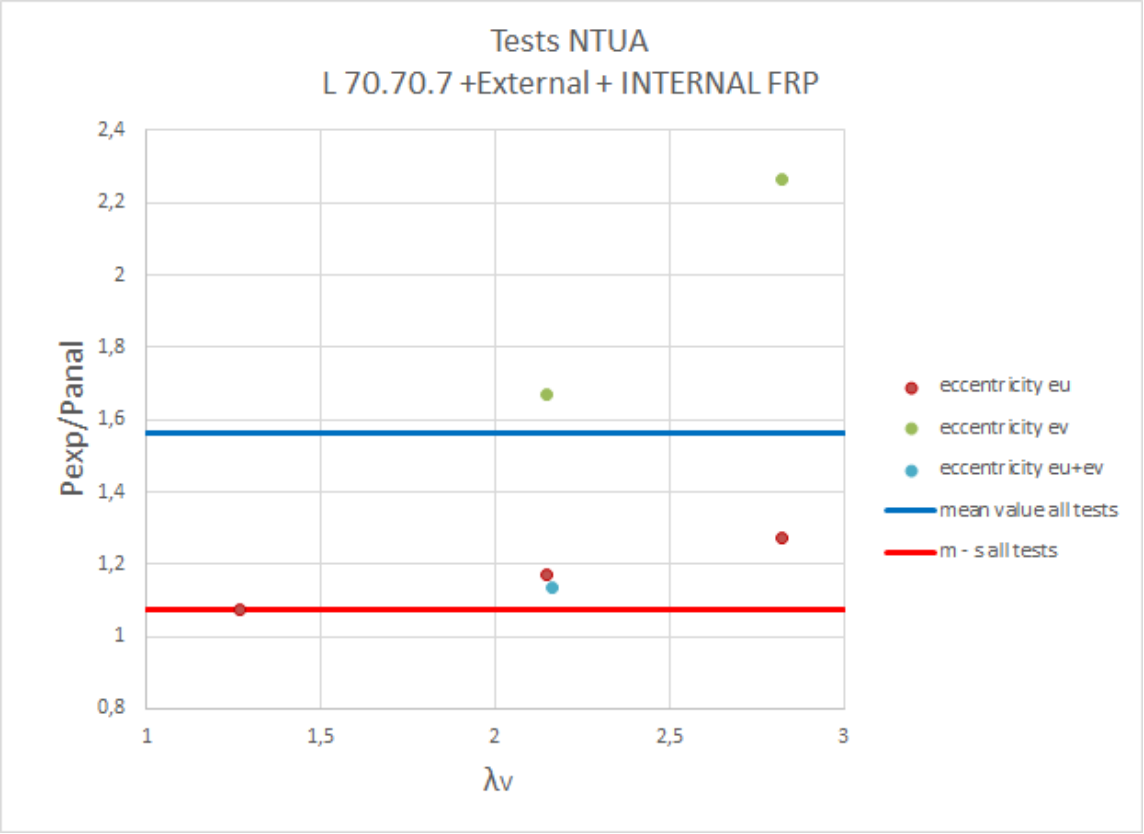

Figure 6.15: Ratio between experimental and analytical ultimate load. Specimens with external + internal FRPs

Fig. 6.16 shows for all tests the experimental ultimate load vs the correspondent analytical one determined by the proposed formulae.

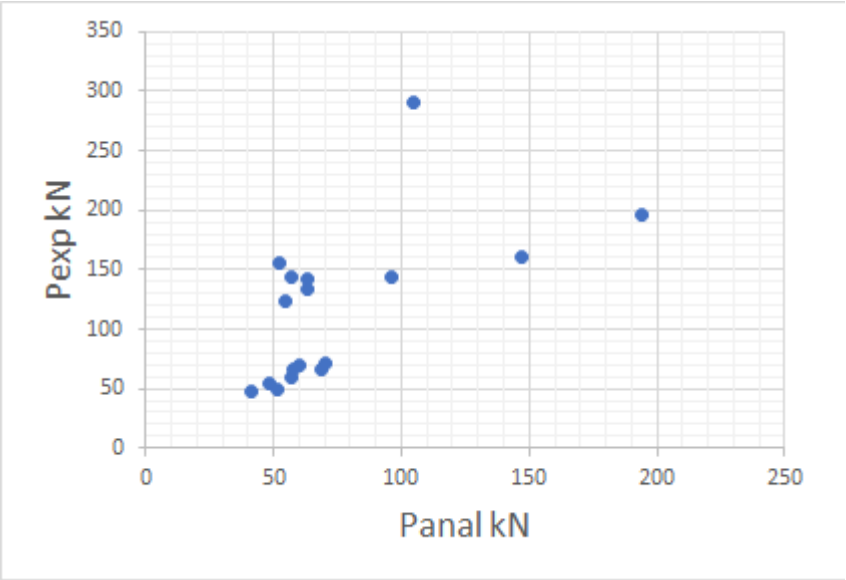

Figure 6.16: Experimental vs analytical ultimate load

Tables 6.1 and 6.2 present the ultimate loads as determined in the tests and by the analytical formula. It may be seen that the predicted load is always but in two tests on the safe side.

The statistical evaluation shows that the ratio P_{exp}/P_{anal} has a mean value m = 1,58, a standard deviation s = 0,522 and a m-s = 1,06.

Table 6.1: Experimental and analytical loads for the compression tests T2 with external+internal strengthening

Specimen	**C-SS1-T2-F**	**C-S4-T2-P**	**C-S6-T2-P**	**C-S8-T2-P**	**C-L4-T2-P**	**C-L6-T2-P**	**C-L8-T2-F**
Pexp (kN)	196.01	70.8	143.4	66.9	55.11	133.68	142.92
Panal (kN)	194.1	70	96	69	48.4	63	63

Table 6.2: Experimental and analytical loads for the compression tests T1 with external strengthening

Specimen	**C-S1-T1-P**	**C-S2-T1-P**	**C-S3-T1-P**	**C-S5-T1-P**	**C-S7-T1-P**
Pexp (kN)	69.7	291.2	66.1	160.3	58.9
Panal (kN)	60	105	58	147	57

Table 6.2: cont.

Specimen	**C-L1-T1-P**	**C-L2-T1-P**	**C-L3-T1-P**	**C-L5-T1-F**	**C-L7-T1-P**
Pexp (kN)	49	143.3	47.55	124.38	155.35
Panal (kN)	51.7	57.3	41	54.5	52

7 Numerical validation

7.1 Modelling with beam elements

As a first approach numerical analyses of the tests were performed using a commercial software package in which the angles were represented by beam elements. The purpose of this study was to investigate the limits of application and the methods of analysis of a strengthened tower by a commercial software. The analyses were performed using the SOFISTIK software package [1].

The material properties for steel in regard to the yield stress and ultimate stress were as the actual measured values of the test specimens. The stress-strain curve was idealized to be bilinear adopting the engineering values of stress and strain, Fig. 7.1. The curve has an elastic branch up to the yield stress and a strain hardening branch. The modulus of elasticity was set equal to E_s = 210 GPa, while the strain hardening modulus equal to 1/150 of the elastic one.

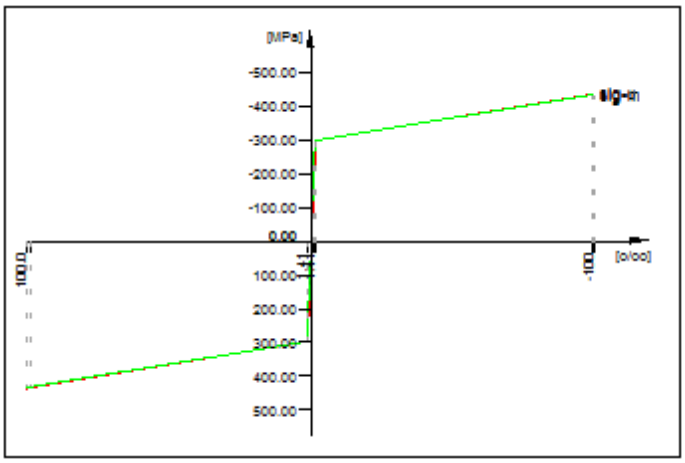

Figure 7.1: Stress-strain curve for steel in numerical analysis

The stress-strain curve for the FRP was linear with modulus of elasticity equal to the nominal value E_f = 170 GPa. The material strength for tension was adopted equal to the nominal value f_f = 3100 MPa, while for compression 1/3 of it f_{fc} = 3100/3 MPa, Fig. 7.2.

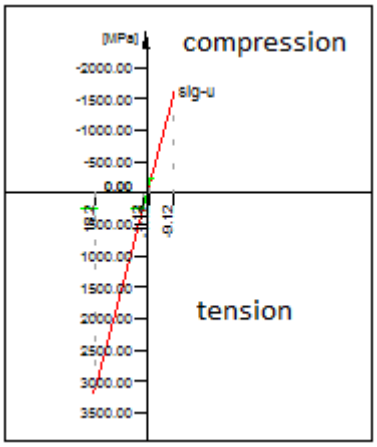

Figure 7.2: Stress-strain curve for FRP in numerical analysis

The cross sections were composed of the steel section L 70.70.7 and the FRP plates of width 50 mm and thickness 1.2 mm, Fig. 7.3 and 7.4. No slip was possible between the steel and the FRP material.

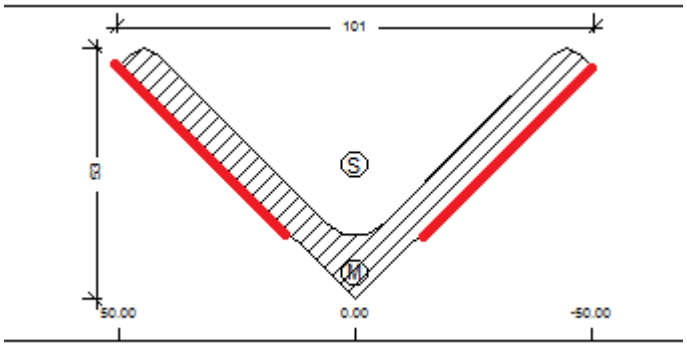

Figure 7.3: Cross section with external FRPs – Specimens T1

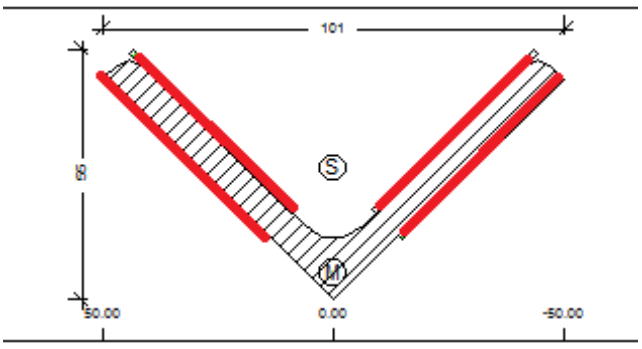

Figure 7.4: Cross section with external and internal FRPs – Specimens T2

7.1.1 Bending tests

The tested specimens were represented by 7 DOF (degree of freedom) beam elements, Fig. 7.5. The end supports corresponded to fork support conditions. The axial displacements were fixed in one end and free in the other end to not allow catenary action. Lateral displacements were restrained near the

middle as in the tests. Similar to the tests, the load was introduced for weak axis bending at the centroid, while for geometric axis bending it was introduced directly at the web. Torsional effects were restrained due to the adopted support conditions. Geometrical and material non-linear analysis was performed up to the attainment of the ultimate load beyond which no convergence could be achieved. This was due to instability, possibly local buckling of the cross section.

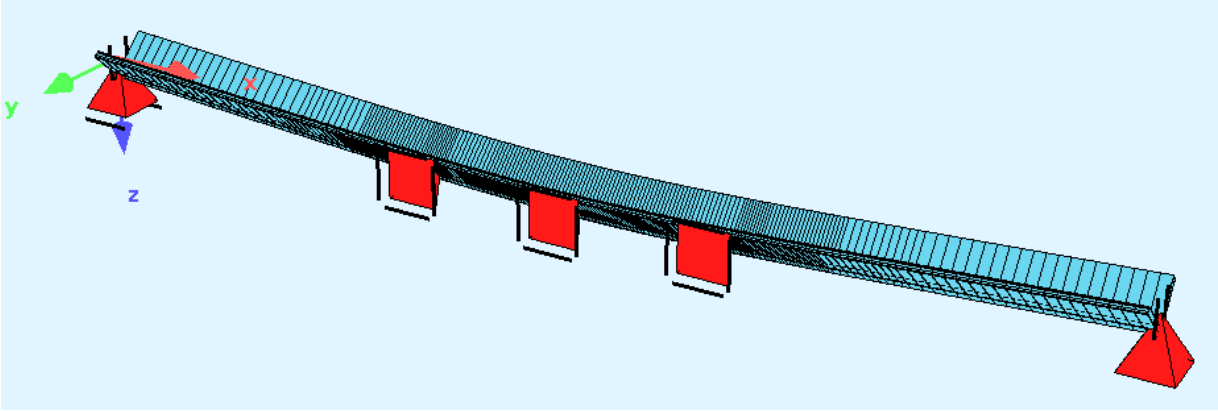

a)

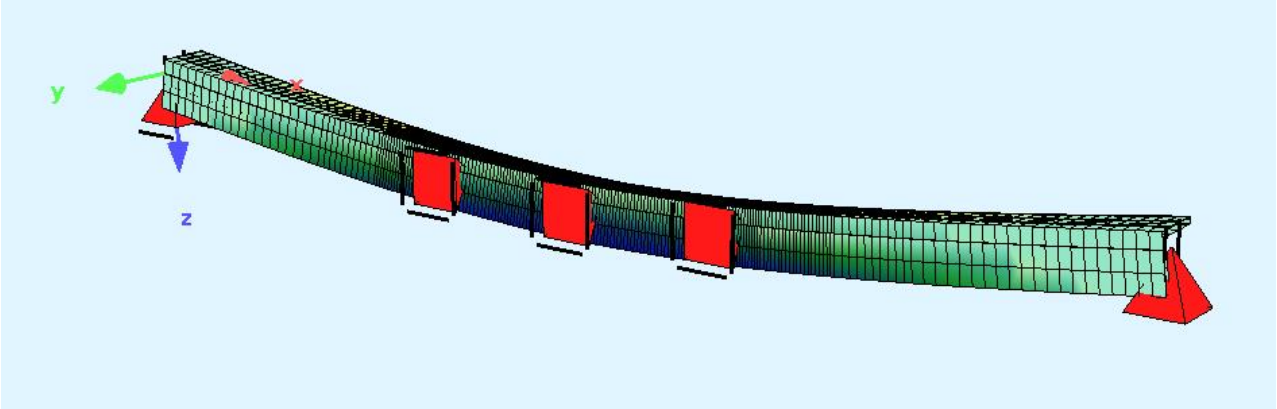

b)

Figure 7.5: Numerical model of the specimens a) in weak and b) in geometrical axis bending

Figs 7.6 and 7.7 illustrate analysis results in the form of load-deflection curves. The numerical curves were nonlinear, mainly due to yielding of steel, with similar shapes to the experimental ones. The elastic stiffness is represented accurately for weak axis bending indicating no slip between steel and FRP material. For geometric axis bending the experimental model is a little softer, possibly due to small rotations of the specimen. The calculated ultimate loads were equal or smaller than the experimental loads, except the doubly strengthened specimen in weak axis bending. However, the numerical models could not predict the true reason of failure, i.e. the detachment of the FRP strips from the steel section. This is indicated by the series of unloading steps that exhibit the experimental

curves, each one corresponding to a partial detachment of the FRP strips. The maximal ultimate load is attained just before the appearance of the first unloading.

As a conclusion it may be said that the numerical beam model accurately predicts the hybrid element behavior in the elastic range. This is due to lack of slip between steel and FRP materials. However, this model is not able to correctly predict the ultimate load because a) it is not able to simulate local buckling as it is based on beam elements that keep the cross section form unchanged and b) no damage rule is implemented in the model that may simulate the detachment of the FRP strips from the steel surface.

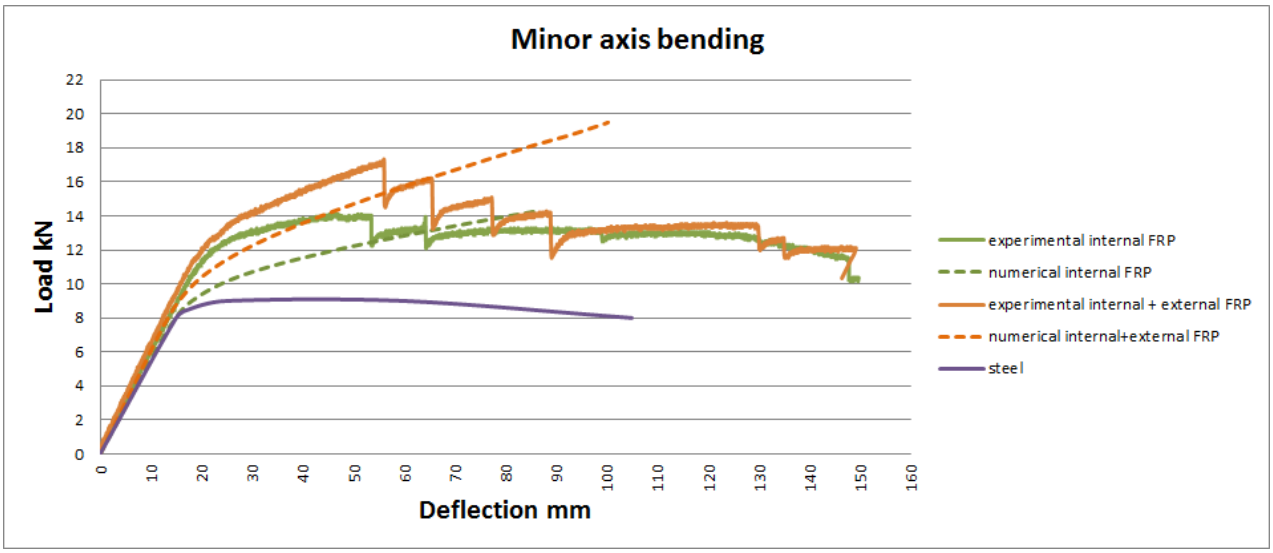

Figure 7.6: Experimental-numerical load-deflection curves. Minor axis bending

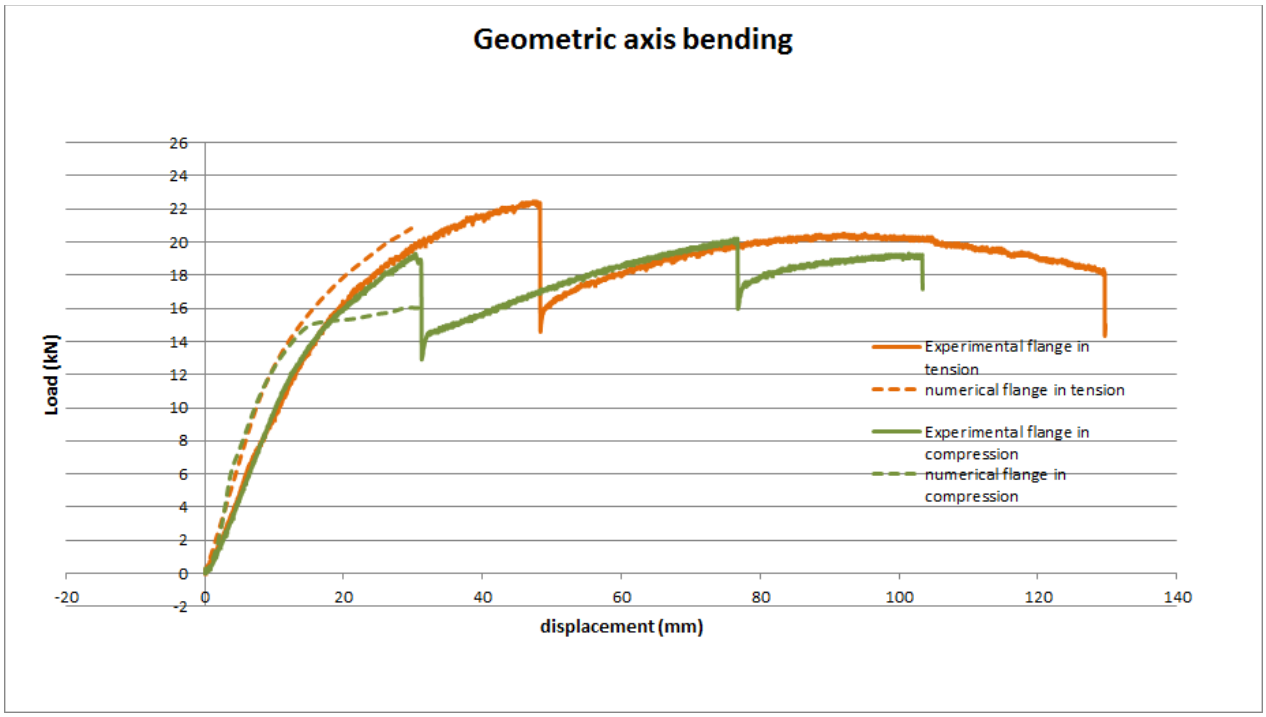

Figure 7.7: Experimental-numerical load-deflection curves. Geometric axis bending

7.1.2 Compression tests

The tested specimens were represented by 7 DOF (degree of freedom) beam elements, Fig. 7.8. The end supports represented fork support conditions. The axial displacements were free at both ends and fixed at mid-span to allow symmetrical response. Rotations were unrestrained at span. Concentrated loading with the relevant eccentricity was introduced at both ends. 2nd order geometrical and material non-linear analysis was performed up to the attainment of the ultimate load beyond which no convergence could be achieved. This was due to global instability.

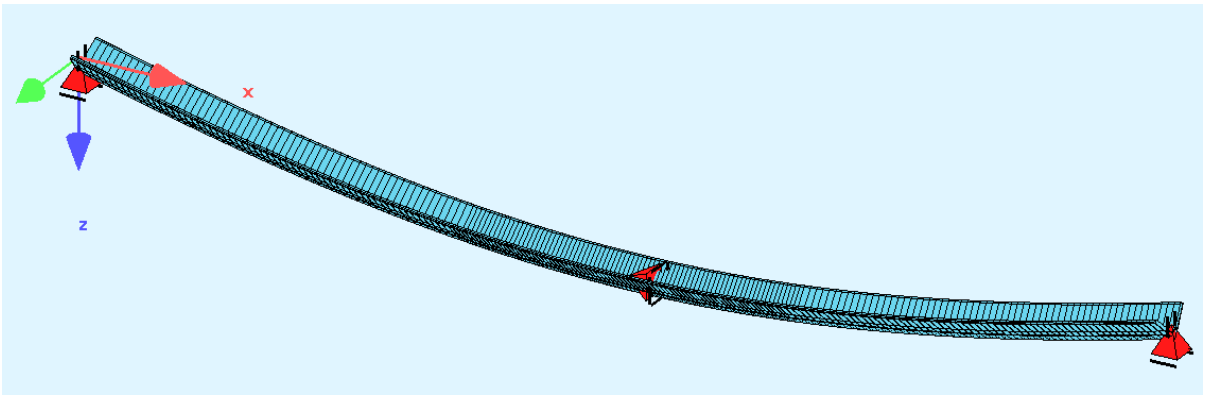

Figure 7.8: Numerical model of the specimens to compression

Figs 7.9 and 7.10 illustrate load-deflection curves in direction of the two principal axes. To allow comparison, the specimens with similar weak axis eccentricities and negligible strong axis eccentricities were selected. The curves well represent the cross section and member properties. The failure loads decrease with increasing slenderness and are higher for double strengthening, specimens T2, compared with single external strengthening, specimens T1. Despite the fact that loading eccentricity produces strong axis bending and therefore deflections in direction of the weak axis, the specimens buckle at failure towards the strong axis producing. At higher loading steps the strong axis deflections, δu, exhibit highly non-linear behavior, while the weak axis deflections, δv, are more or less linear over the entire loading range. This is illustrated in Fig. 7.11 which shows the two deflections for one specimen.

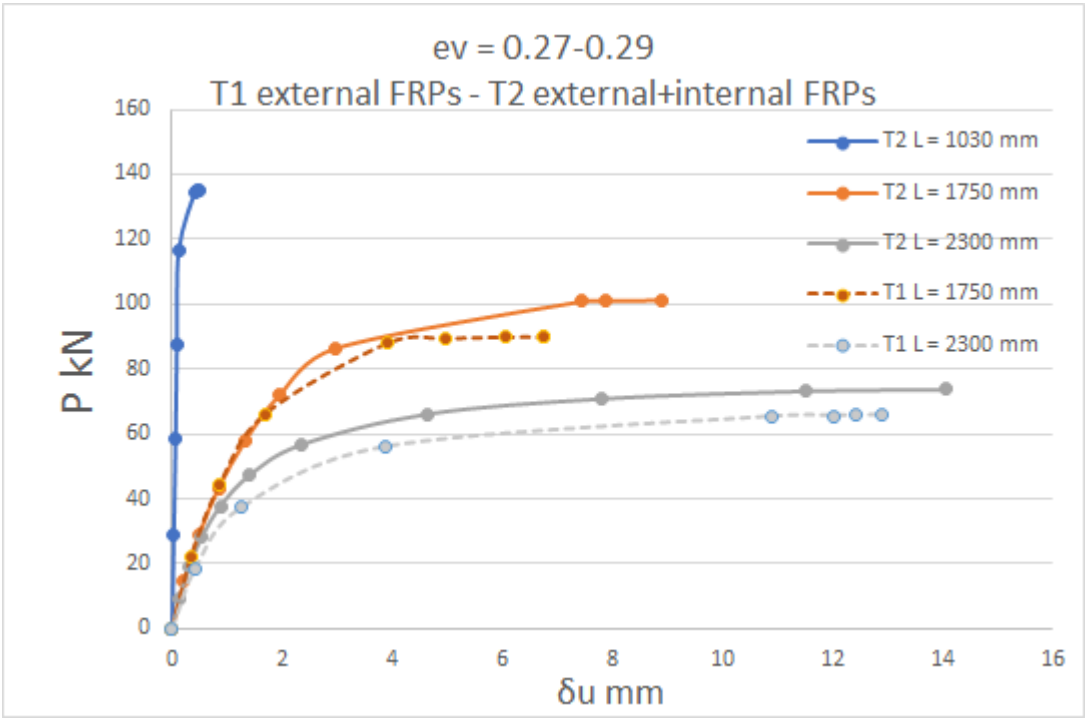

Figure 7.9: Numerical load-deflection curves in direction of the strong axis

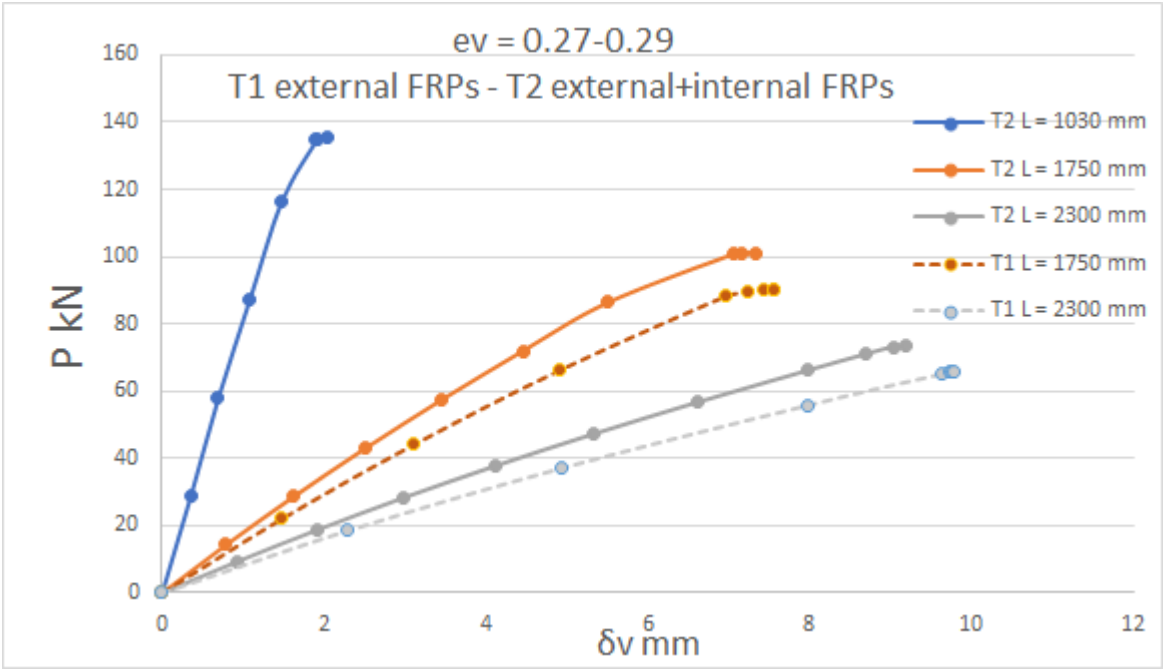

Figure 7.10: Numerical load-deflection curves in direction of the weak axis

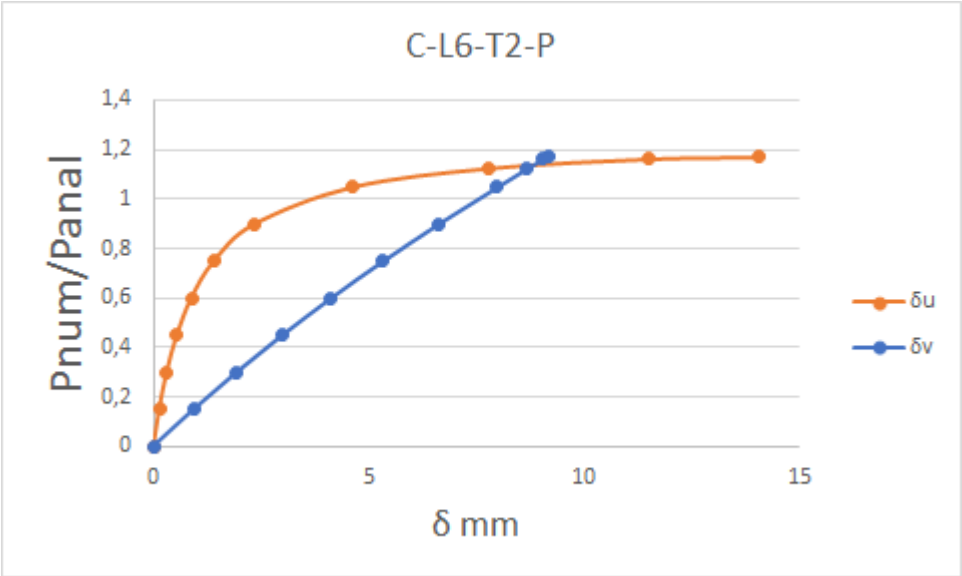

Figure 7.11: Numerical load-deflection curves in direction of the weak axis

Fig. 7.12 shows for all tests the experimental ultimate load vs the correspondent numerical one determined by numerical non-linear analysis using the SOFISTIK software, while Fig. 7.13 the analytical vs. numerical ultimate loads.

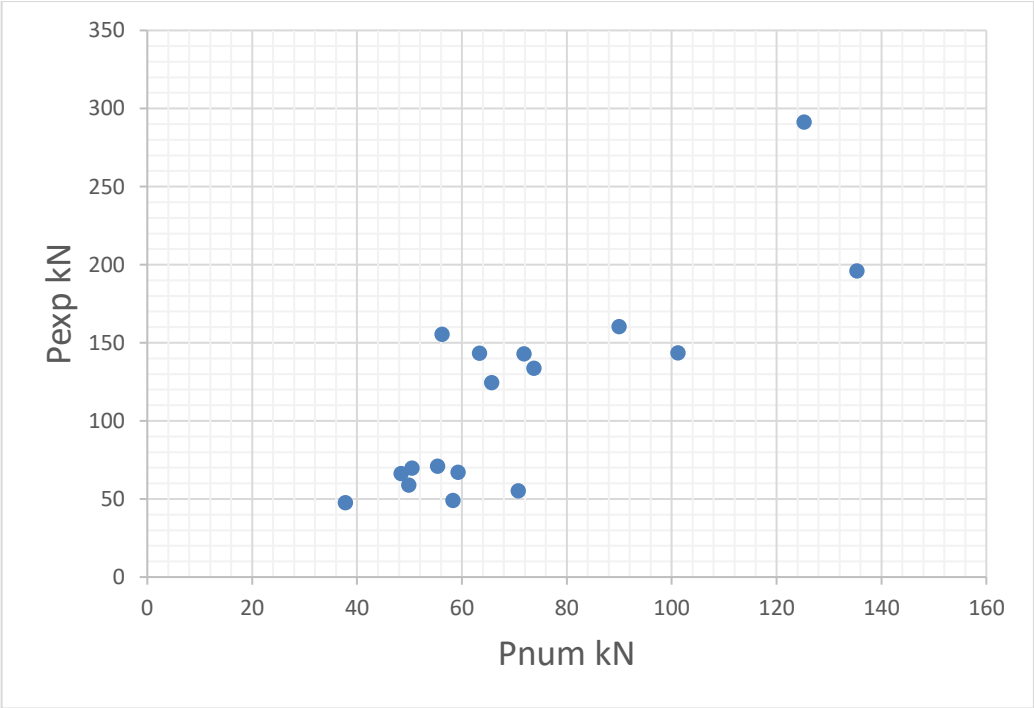

Figure 7.12: Experimental vs numerical ultimate load using beam element models

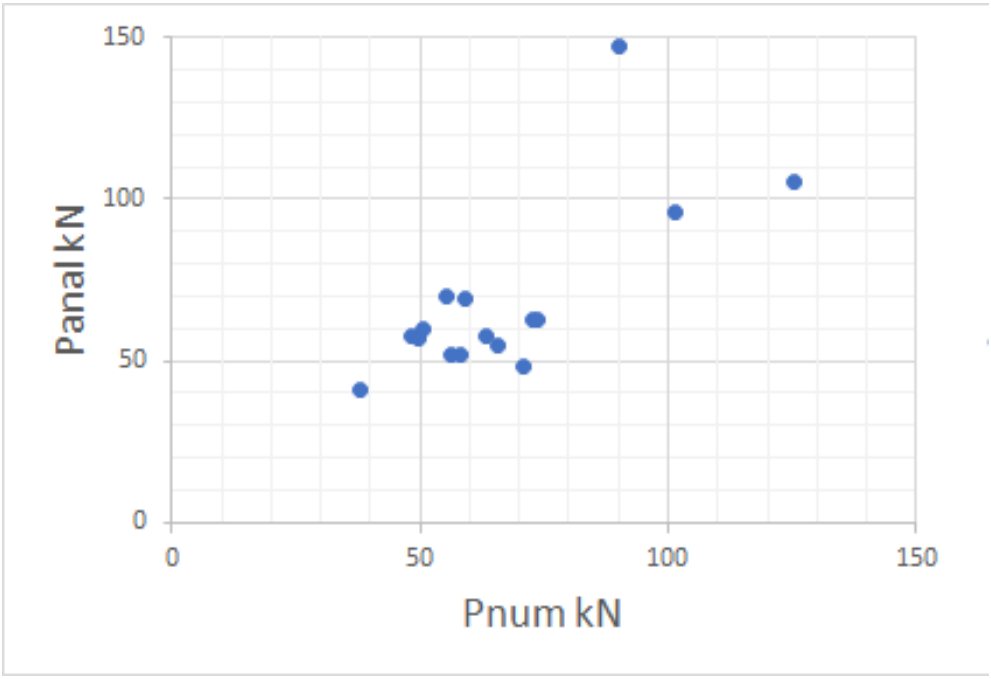

Figure 7.13: Experimental vs numerical ultimate load using beam element models

Tables 7.1 and 7.2 present the experimental, analytical and numerical ultimate loads, while Table 7.3 the statistical evaluation for the ratios between experimental, analytical and numerical loads. It may be seen that the predicted load is always but in two tests on the safe side.

The statistical evaluation shows that the ratio P_{exp}/P_{anal} has a mean value m = 1,58, a standard deviation s = 0,522 and a m-s = 1,06.

Table 7.1: Experimental, analytical and analytical loads for the compression tests T2 with external+internal strengthening

Specimen	**C-SS1-T2-F**	**C-S4-T2-P**	**C-S6-T2-P**	**C-S8-T2-P**	**C-L4-T2-P**	**C-L6-T2-P**	**C-L8-T2-F**
Pexp (kN)	196.01	70.8	143.4	66.9	55.11	133.68	142.92
Panal (kN)	194.1	70	96	69	48.4	63	63
Pnum (kN)	135.2877	55.37	101.184	59.271	70.7608	73.71	71.82

Table 7.2: Experimental, analytical and analytical loads for the compression tests T1 with external strengthening

Specimen	**C-S1-T1-P**	**C-S2-T1-P**	**C-S3-T1-P**	**C-S5-T1-P**	**C-S7-T1-P**
Pexp (kN)	69,7	291,2	66,1	160,3	58,9
Panal (kN)	60	105	58	147	57
Pnum (kN)	50,46	125,265	48,372	89,964	49,875

Table 7.2 cont.

Specimen	C-L1-T1-P	C-L2-T1-P	C-L3-T1-P	C-L5-T1-F	C-L7-T1-P
Pexp (kN)	49	143,3	47,55	124,38	155,35
Panal (kN)	51,7	57,3	41	54,5	52
Pnum (kN)	58,31	63,3386	37,7547	65,67264	56,2367

Table 7.3 gives the statistical evaluation for the ratios between experimental, analytical and numerical loads. It may be seen that the experimental load is in the mean around 60% higher than both analytical and numerical load, while the analytical and numerical loads are in the mean equal. The numerical analysis gives lower standard deviation to the experimental load compared to the analytical one, leading to a higher value of m-s. However, this is due to the fact that the experimental loads where much higher than those calculated by the analytical formula or the numerical analysis. In all tests all but one achieved in the experiments lower loads compared to the analytical or numerical ones.

Table 7.3: Statistical evaluation between experimental, analytical and analytical loads for the compression tests

	Mean value m	Standard deviation s	m - s
Pexp/Pnum	1.58	0.523	1.06
Pnum/Panal	1.00	0.211	0.79
Pexp/Panal	1.59	0.695	0.90

7.2 Modelling with FEM using volume elements

In a second approach FEM analyses of the bending tests were performed using volume elements. The analyses were performed by application of the ABAQUS software package [12].

The stress-strain curve of steel followed the experimental one from the coupon tests using point-by-point the engineering values for stress and strain, Fig. 7.13. The stress-strain curve for the FRP strips were linear up to the maximum stress 3100 MPa with a modulus of elasticity 170 GPa. The adhesive was not included in the model.

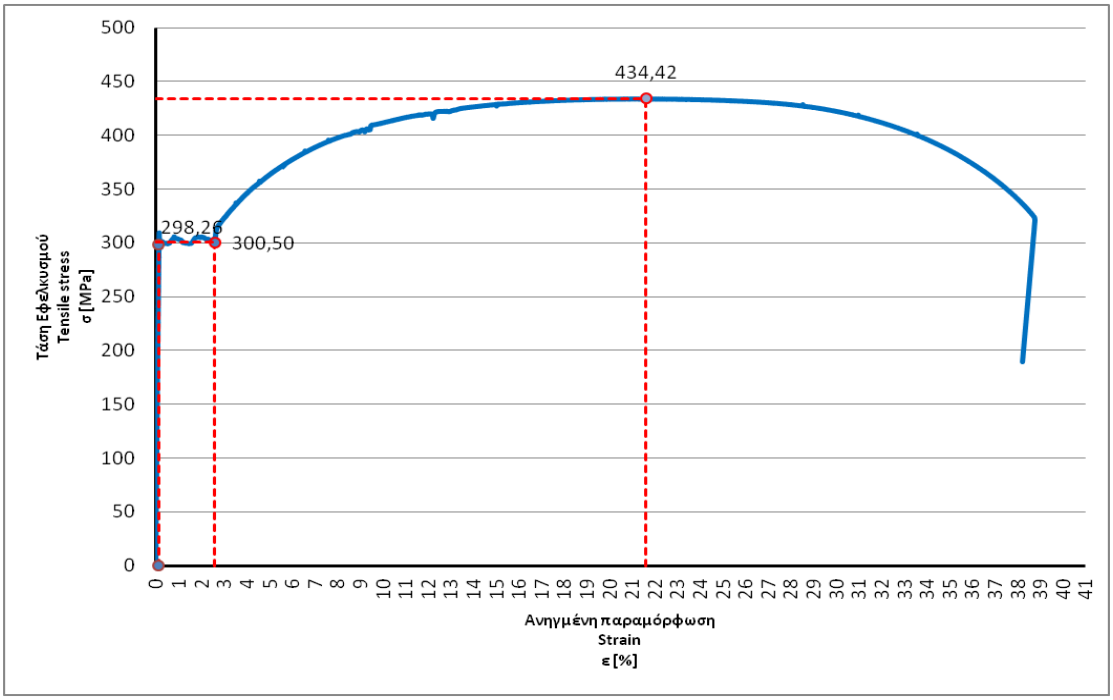

Figure 7.14: Stress-strain curve for steel in FEM analysis

The representation of the angle section and the FRP plates was by means of volume elements, Fig. 7.14.

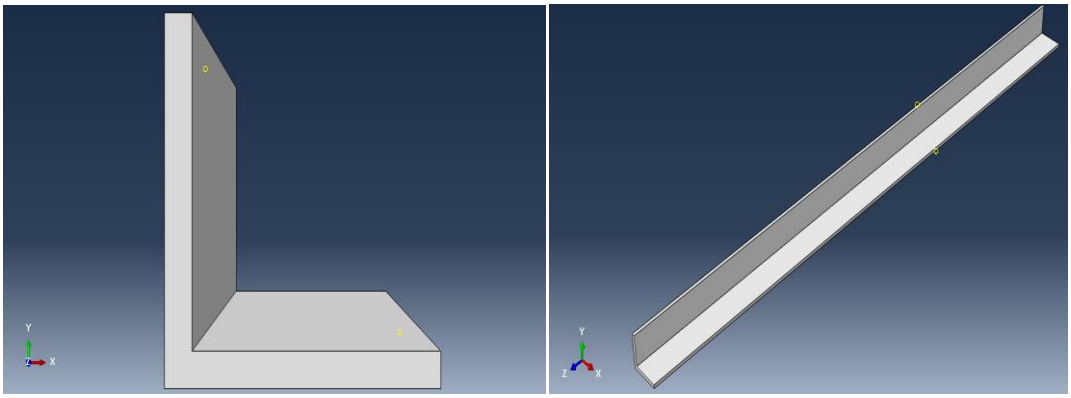

Figure 7.15: Representation of steel section and FRP plates with volume elements

The load conditions were introduced by definition of a reference node on which the displacements were applied. All other nodes in the relevant cross section were coupled to this reference node. The support conditions were such to restrain the displacements along the axes x, y and the rotations around the axes y,z at the ends, Fig. 7.15.

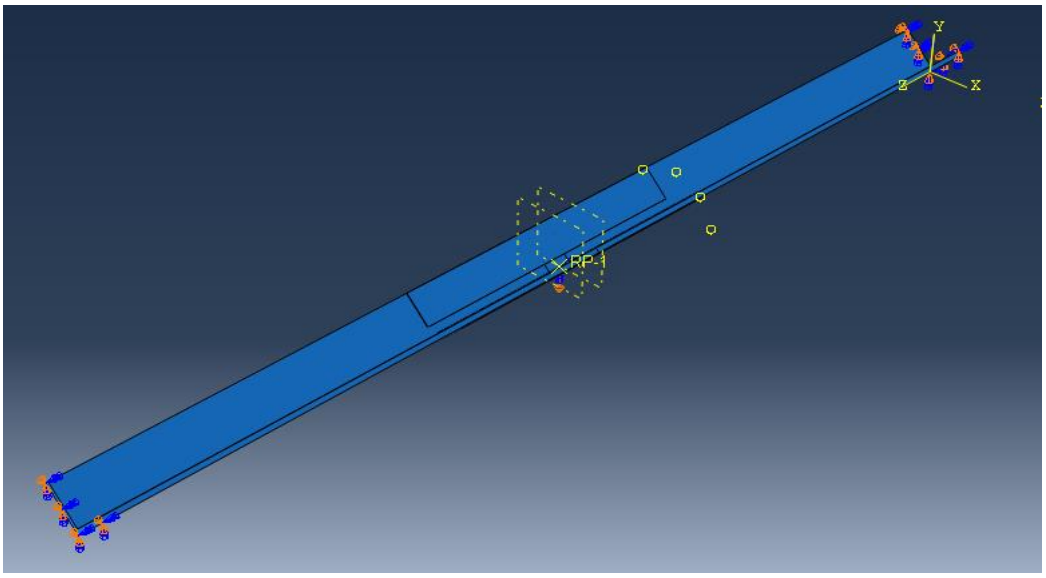

Figure 7.16: Loading and support conditions for specimen B-T2-V

The discretization was by means of hexahedral finite elements with 8-nodes, type C3D8R. Three elements along the thickness were used, leading to elements lengths 18 mm for the angle section and 10 mm for the FRP strips, Fig. 7.16. This was proven sufficient by iterative analysis with more elements. The connection between the two materials was by rigid tie constrains, without consideration of the adhesive resin.

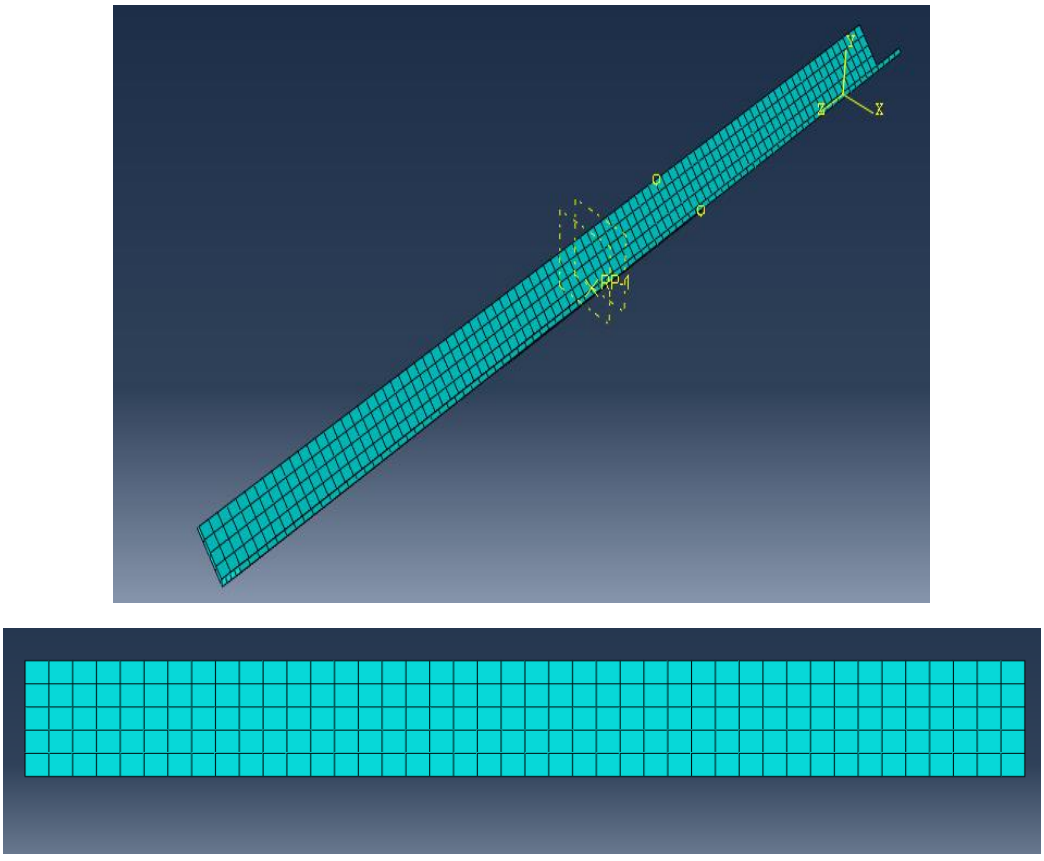

Figure 7.17: Discretization of the steel section and the FRP strips.

The connection between the two materials was by rigid tie constrains, without consideration of the adhesive resin. Figs. 7.16 and 7.17 show the pictures of the displaced specimen at failure load, and Fig. 7.18 pictures of the v. Mises stresses for the FRP strips.

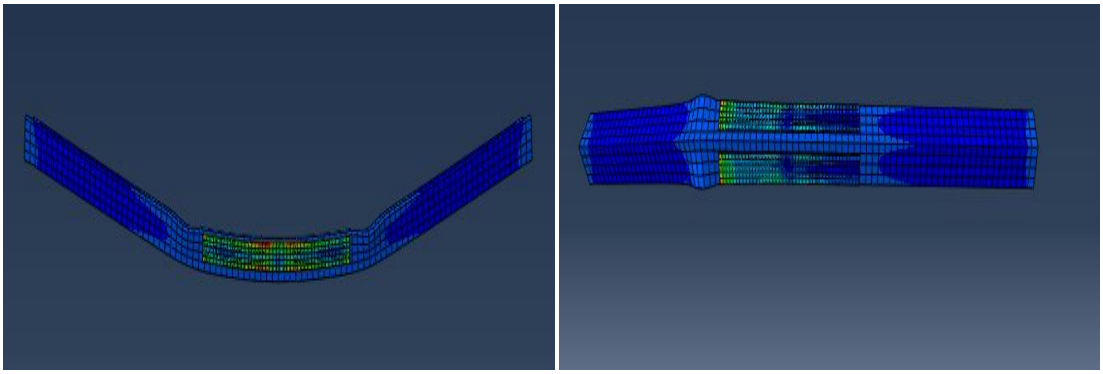

a) **b)**

Figure 7.18: Weak axis bending. Deformed state of specimens at failure a) Specimen B-T1-V b) Specimen B-T2-V

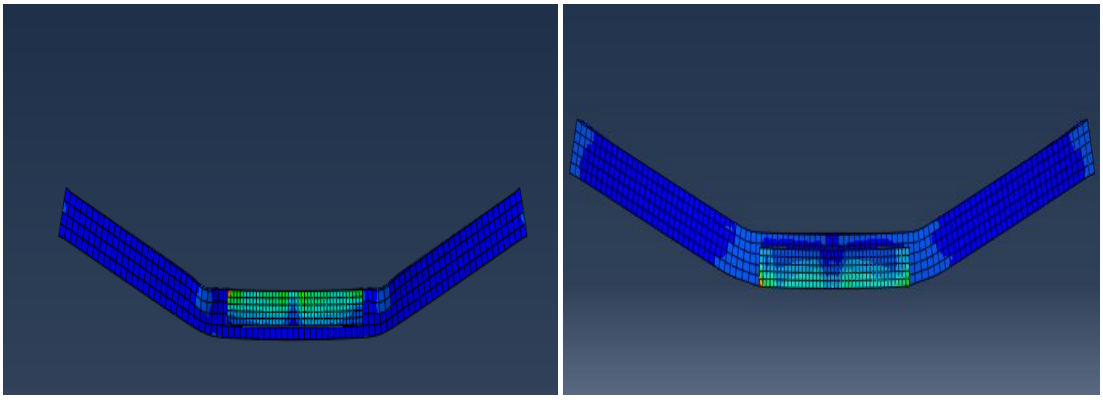

a) **b)**

Figure 7.19: Geometric axis bending. Deformed state of specimens at failure a) Specimen B-T1-L b) Specimen B-T2-LI

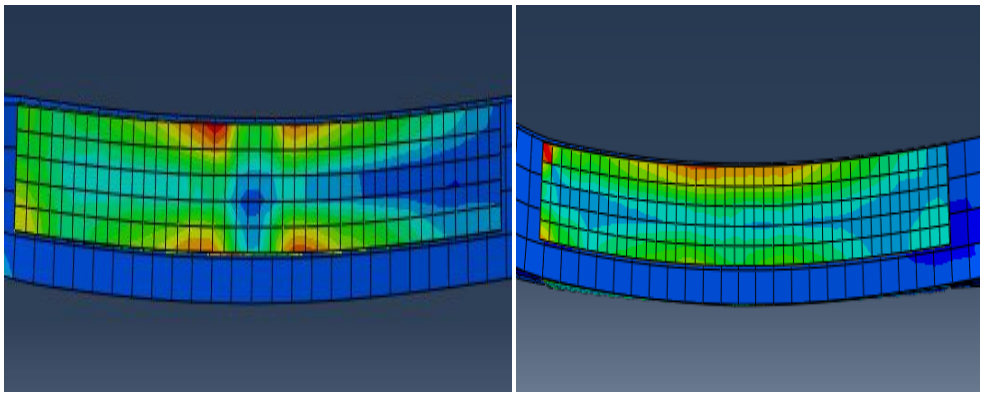

Figure 7.20: v. Mises stresses of the FRP strips

Figs. 7.19 to 7.22 illustrate load – deflection experimental and numerical curves. The numerical calculation represents well the behavior in the elastic range, but not the one in the post-elastic range, nor the detachment of the FRP strips from the steel surface. Like in the beam models, this is due to the lack of implementation of a damage criterion that includes the adhesive and the FRP material. Accordingly, the numerical analysis with the models used cannot predict with higher accuracy the ultimate loads.

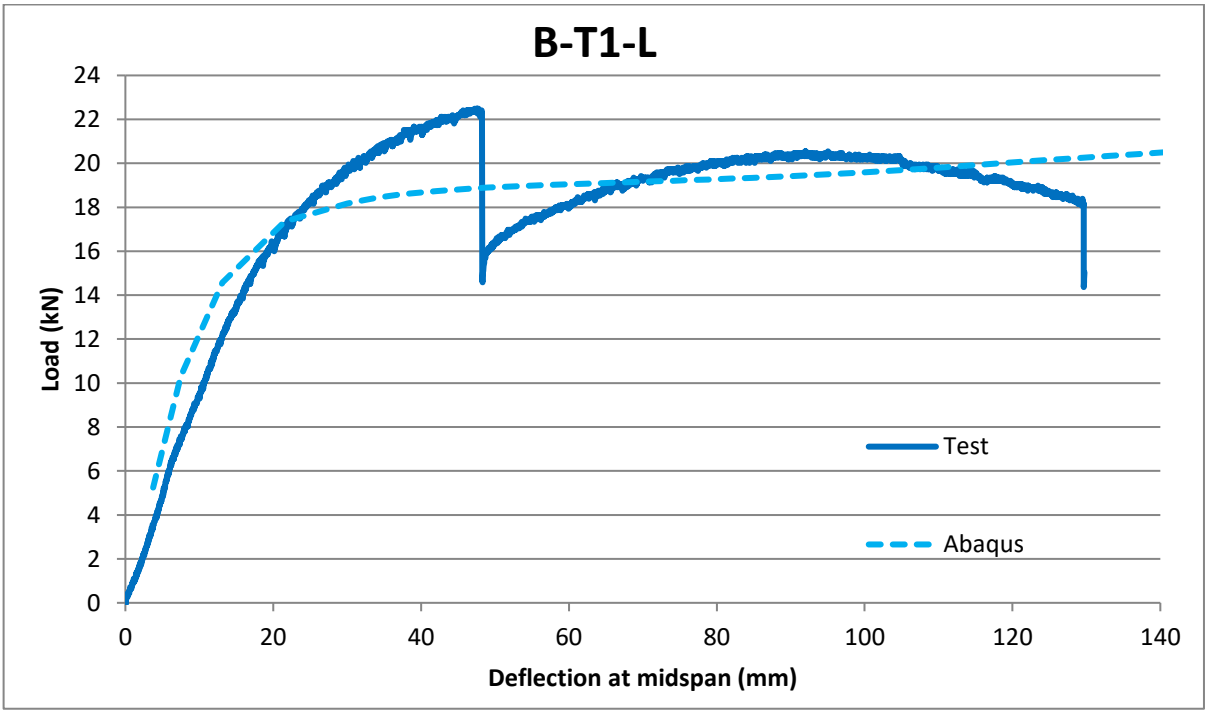

Figure 7.21: Experimental-numerical load-deflection curves. Geometric axis bending. Specimen B-T1-L

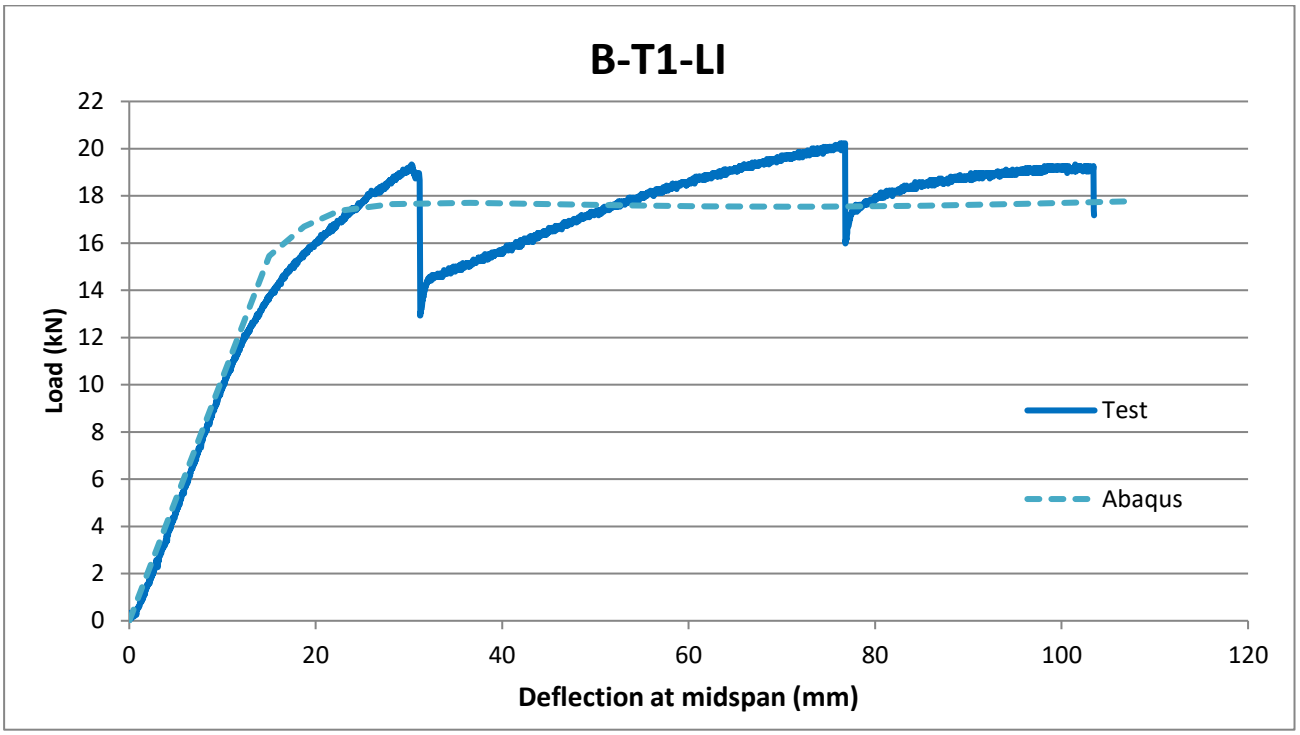

Figure 7.22: Experimental-numerical load-deflection curves. Geometric axis bending. Specimen B-T1-LI

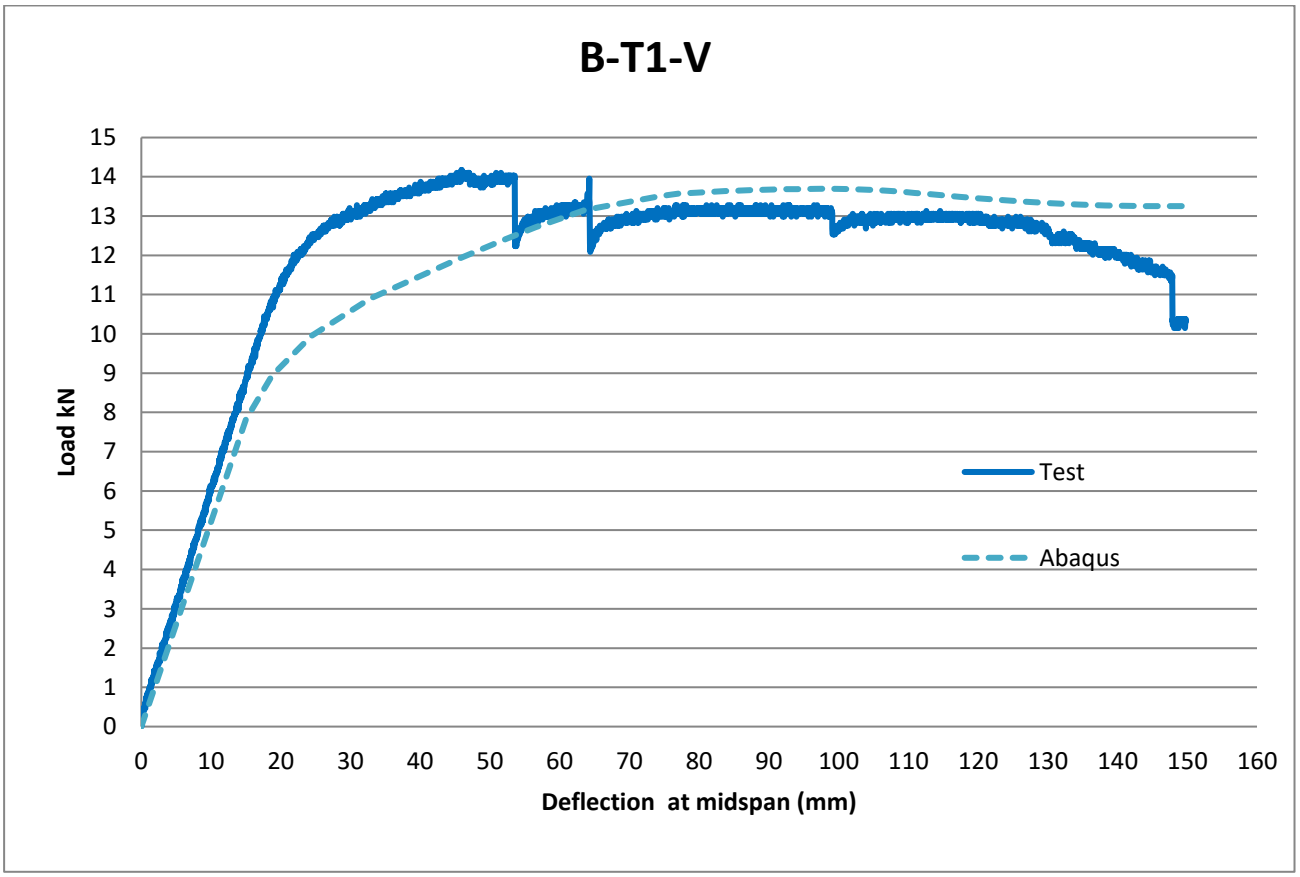

Figure 7.23: Experimental-numerical load-deflection curves. Weak axis bending. Specimen B-T1-V

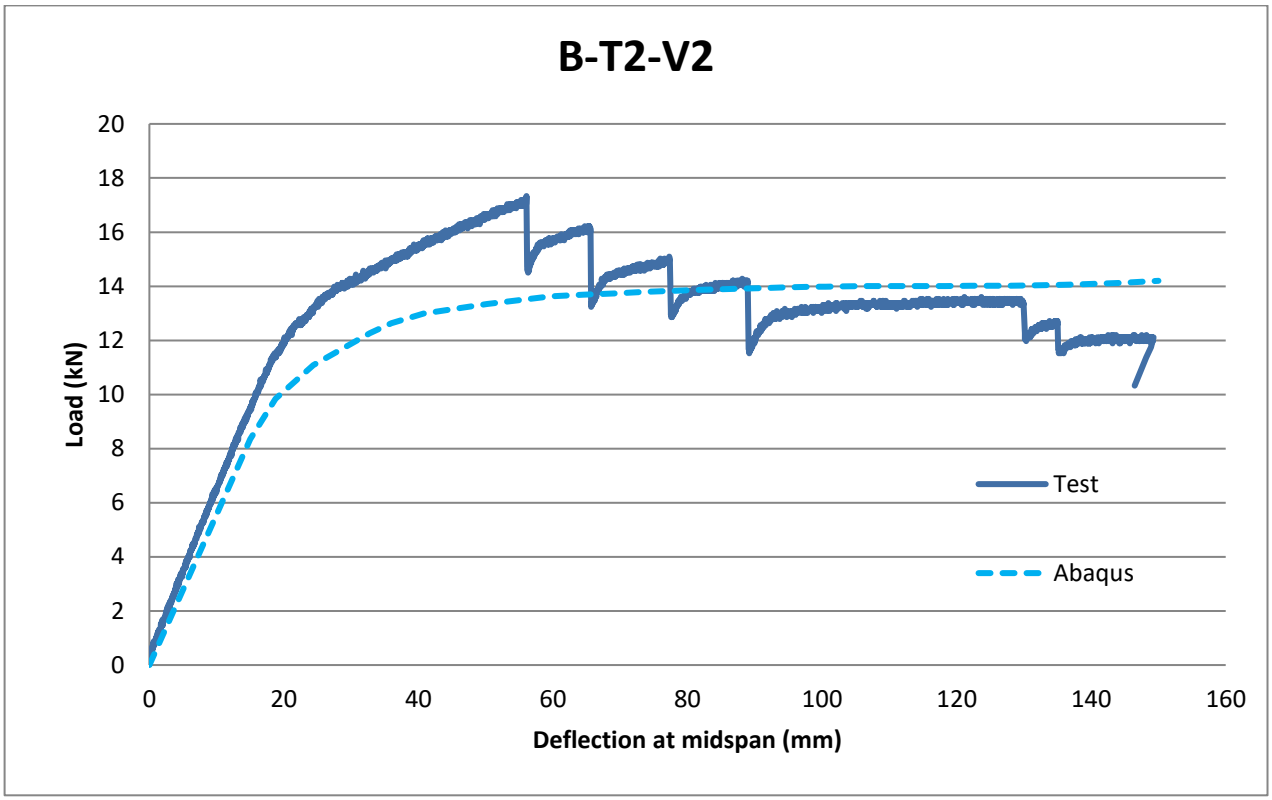

Figure 7.24: Experimental-numerical load-deflection curves. Weak axis bending. Specimen B-T2-V2

8 Conclusions

Analytic expressions for the cross-section properties were derived for hybrid cross-sections composed of equal angle profiles and FRP plates applied externally or externally and internally to the legs. Analytic formulae were proposed for design of members composed from such cross-sections when subjected to combined loading. The assumptions made were as following:

- The shear connection between the two materials - steel and FRP – is full, with no slip between them.
- Local buckling of the angle steel walls is not present.
- The steel stress at ultimate limit states is always equal to the yield strength.
- For bending, the FRP stress at ultimate limit states is equal to the nominal tensile strength of the FRP material.
- For compression force, the FRP stress at ultimate limit states is equal to ½ of the nominal tensile strength of the FRP material.
- For tension force, the FRP stress at ultimate limit states is equal to the nominal tensile strength of the FRP material.
- At the design bending moment steel material is fully plastic, while FRP material fully elastic.
- The axial force – bending interaction is linear for tension force and non-linear for compression force.

Numerical analyses were performed in which the systems were represented by beam elements and volume FEM. The analytic formulae and the numerical analyses were validated against the experimental bending and compression tests that have been carried out during the current research project. It was shown that the analytical formulae provide safe predictions for the hybrid elements. Although the level of accuracy is variable, the analytical formulae are useful tools to predict the resistance of such hybrid members. Additionally, it was shown that the present numerical models, without implementation of a damage criterion, are able to represent well the elastic behavior but not the behavior near the limit load. For that purpose, it is recommended to be used for material linear analysis, in combination with the analytic formula for member design.

References

[1] EN 1993-1-1 (2005) Eurocode 3: Design of steel structures - Part 1-1: General rules and rules for buildings. CEN

[2] EN 1993-3-1 (2006) Eurocode 3: Design of steel structures - Part 3-1: Towers, masts and chimneys – Towers and masts. CEN

[3] Technical Report n°55, Third Edition (2012): Design guidance for strengthening concrete structures using fibre composite materials, based on Eurocode 2, part 1-1 (England).

[4] AFGC (2011): Réparation et Renforcement des Structures en béton au moyen des Matériaux Composites, based on Eurocode 2, part 1-1 (France).

[5] CNR-DT 200 R1 (2013): Istruzioni per la Progettazione, l'Esecuzione ed il Controllo di Interventi di Consolidamento Statico mediante l'utilizzo di Compositi Fibrorinforzati (Italy).

[6] CNR-DT 202 (2005), Guidelines for the Design and Construction of Externally Bonded FRP Systems for Strengthening Existing Structures, Rome

[7] Fib 14 (2001) : Design and use of externally bonded fibre reinforced polymer reinforcement (FRP EBR) for reinforced concrete structures, based on Eurocode 2, part 1-1 (Switzerland).

[8] Cadei JMC, Stratford TJ, Hollaway LC, Duckett WG. Strengthening metallic structures using externally bonded fibre-reinforced polymers. London: CIRIA; 2004.

[9] Design Manual for Roads and Bridges, Volume 1 Highway Structures: Approval Procedures and General Design, Section 3 General Design, Part 18 Strengthening Highway Structures Using Externally Bonded Fibre Reinforced Polymer, 2008 (United Kingdom).

[10] ANGELHY – Deliverable 2.2 (1019) - Report proposing design rules for single angle members.

[11] SOFISTIK, Finite Element Software, www.sofistik.com

[12] ABAQUS 6.13 documentation, Simulia, Dassault Systemes.

List of Figures

Figure 2.1: Notation, principal and geometric axes for equal angle section 4

Figure 2.2: Notation and principal axes for hybrid section 5

Figure 2.3: Strain and stress diagrams for elastic moment weak axis 6

Figure 2.4: Strain and stress diagrams for elastic moment strong axis 7

Figure 2.5: Stress diagram for limit elastic-plastic moment, weak axis 7

Figure 2.6: Stress diagram for limit elastic-plastic moment, strong axis 9

Figure 2.7: Notation and geometric axes for hybrid section 10

Figure 2.8: Stresses at the steel profile for moment on the geometric axis, leg in compression 11

Figure 2.9: Stresses at the steel profile for moment on the geometric axis, leg in tension 11

Figure 2.10: Stresses for elastic-plastic moment geometric axis, leg in compression 12

Figure 2.11: Stresses for elastic-plastic moment geometric axis, leg in tension 13

Figure 6.1: Limit FRP strain at maximal load, specimen B-T1-V 23

Figure 6.2: Experimental vs analytical load –deflection curves for bending on the weak axis, hybrid section with external FRP 23

Figure 6.3: Limit FRP strain at maximal load, specimen B-T2-V2 24

Figure 6.4: Experimental vs analytical load –deflection curves for bending on the weak axis, hybrid section with external + internal FRP 24

Figure 6.5: Limit FRP strain at maximal load, specimen B-T1-L 25

Figure 6.6: Experimental vs analytical load –deflection curves for bending on the geometric axis. Leg in tension. Hybrid section with external FRP 25

Figure 6.7: Limit FRP strain at maximal load, specimen B-T1-L1 26

Figure 6.8: Experimental vs analytical load –deflection curves for bending on the geometric axis. Leg in compression. Hybrid section with external FRP 26

Figure 6.9: Position of the cross-section centroid. Analytical (blue) vs experimental from strain measurements (green). Bending around the geometric axis, leg in tension. SG in black are attached to steel, SG in magenta are attached to FRP 28

Figure 6.10: Position of the cross-section centroid. Analytical (blue) vs experimental from strain measurements (green). Bending around the geometric axis, leg in compression. SG in black are attached to steel, SG in magenta are attached to FRP 29

Figure 6.11: Position of the cross-section centroid. Analytical (blue) vs experimental from strain measurements (green). Bending around the weak axis, external FRP. SG in black are attached to steel, SG in magenta are attached to FRP.....29

Figure 6.12: Position of the cross-section centroid. Analytical (blue) vs experimental from strain measurements (green). Bending around the weak axis, eternal + internal FRP. SG in black are attached to steel, SG in magenta are attached to FRP.....30

Figure 6.13: Position of the cross-section centroid. Analytical (blue) vs experimental from strain measurements (green). Bending around the weak axis, eternal + internal FRP. SG in black are attached to steel, SG in magenta are attached to FRP.....30

Figure 6.14: Ratio between experimental and analytical ultimate load. Specimens with external FRPs.....32

Figure 6.15: Ratio between experimental and analytical ultimate load. Specimens with external + internal FRPs.....32

Figure 6.16: Experimental vs analytical ultimate load.....33

Figure 7.1: Stress-strain curve for steel in numerical analysis.....34

Figure 7.2: Stress-strain curve for FRP in numerical analysis.....35

Figure 7.3: Cross section with external FRPs – Specimens T1.....35

Figure 7.4: Cross section with external and internal FRPs – Specimens T2.....35

Figure 7.5: Numerical model of the specimens a) in weak and b) in geometrical axis bending.....36

Figure 7.6: Experimental-numerical load-deflection curves. Minor axis bending.....37

Figure 7.7: Experimental-numerical load-deflection curves. Geometric axis bending.....37

Figure 7.8: Numerical model of the specimens to compression.....38

Figure 7.9: Numerical load-deflection curves in direction of the strong axis.....39

Figure 7.10: Numerical load-deflection curves in direction of the weak axis.....39

Figure 7.11: Numerical load-deflection curves in direction of the weak axis.....40

Figure 7.12: Experimental vs numerical ultimate load using beam element models.....40

Figure 7.13: Experimental vs numerical ultimate load using beam element models.....41

Figure 7.14: Stress-strain curve for steel in FEM analysis.....43

Figure 7.15: Representation of steel section and FRP plates with volume elements.....43

Figure 7.16: Loading and support conditions for specimen B-T2-V.....44

Figure 7.17: Discretization of the steel section and the FRP strips.....44

Figure 7.18: Weak axis bending. Deformed state of specimens at failure a) Specimen B-T1-V b) Specimen B-T2-V 45

Figure 7.19: Geometric axis bending. Deformed state of specimens at failure a) Specimen B-T1-L b) Specimen B-T2-LI 45

Figure 7.20: v. Mises stresses of the FRP strips 46

Figure 7.21: Experimental-numerical load-deflection curves. Geometric axis bending. Specimen B-T1-L 46

Figure 7.22: Experimental-numerical load-deflection curves. Geometric axis bending. Specimen B-T1-LI 47

Figure 7.23: Experimental-numerical load-deflection curves. Weak axis bending. Specimen B-T1-V 47

Figure 7.24: Experimental-numerical load-deflection curves. Weak axis bending. Specimen B-T2-V2 48

List of Tables

Table 3.1: Different types of application 15

Table 5.1: C_b factor for the determination of the critical LTB moment.....20

Table 6.1: Experimental and analytical loads for the compression tests T2 with external+internal strengthening 33

Table 6.2: Experimental and analytical loads for the compression tests T1 with external strengthening.....33

Table 7.1: Experimental, analytical and analytical loads for the compression tests T2 with external+internal strengthening 41

Table 7.2: Experimental, analytical and analytical loads for the compression tests T1 with external strengthening.....41

Table 7.3: Statistical evaluation between experimental, analytical and analytical loads for the compression tests 42